JOURNAL OF GEOPHYSICAL RESEARCH: SOLID EARTH, VOL. 118, 1–21, doi:10.1002/jgrb.50169, 2013

Bayesian inversion of data from effusive volcanic eruptions using physics-based models: Application to Mount St. Helens 2004–2008

Kyle Anderson[1,2] and Paul Segall[1]

Received 31 August 2012; revised 5 March 2013; accepted 21 March 2013.

[1] Physics-based models of volcanic eruptions can directly link magmatic processes with diverse, time-varying geophysical observations, and when used in an inverse procedure make it possible to bring all available information to bear on estimating properties of the volcanic system. We develop a technique for inverting geodetic, extrusive flux, and other types of data using a physics-based model of an effusive silicic volcanic eruption to estimate the geometry, pressure, depth, and volatile content of a magma chamber, and properties of the conduit linking the chamber to the surface. A Bayesian inverse formulation makes it possible to easily incorporate independent information into the inversion, such as petrologic estimates of melt water content, and yields probabilistic estimates for model parameters and other properties of the volcano. Probability distributions are sampled using a Markov-Chain Monte Carlo algorithm. We apply the technique using GPS and extrusion data from the 2004–2008 eruption of Mount St. Helens. In contrast to more traditional inversions such as those involving geodetic data alone in combination with kinematic forward models, this technique is able to provide constraint on properties of the magma, including its volatile content, and on the absolute volume and pressure of the magma chamber. Results suggest a large chamber of >40 km^3 with a centroid depth of 11–18 km and a dissolved water content at the top of the chamber of 2.6–4.9 wt%.

Citation: Anderson, K., and P. Segall (2013), Bayesian inversion of data from effusive volcanic eruptions using physics-based models: Application to Mount St. Helens 2004–2008, *J. Geophys. Res. Solid Earth*, *118*, doi:10.1002/jgrb.50169.

1. Introduction

[2] Properties of volcanic systems are commonly inferred by using geodetic observations to constrain simple kinematic models. These models do not explicitly include magmatic processes or the ways that such processes give rise to observable fields, and as a result are not well-suited for constraint by diverse time-evolving data sets and cannot be used to directly estimate most properties of the magma in the system. These limitations reduce our ability to leverage observations in the understanding of complex volcanic systems. For instance, while it is possible to use geodetic data with a kinematic model of a spherical magma chamber to constrain the chamber's location and volume change, its total volume and pressure change cannot in general be independently estimated [*McTigue*, 1987], and little insight into properties of the magma and the forces that actually give rise to displacements may be obtained. Such constraint requires additional information and a model that includes at least some physical-chemical properties of the magma [e.g., *Mastin et al*., 2008].

[3] Physics-based forward models can link processes occurring in the magmatic system with diverse observations including ground deformation, extrusion rate, gas emissions, and gravity changes, and therefore allow all observations to be used simultaneously to constrain properties of the volcanic system. Such models are also able in principle to predict the full evolution of an eruption given only initial conditions and material properties, which results in a more relevant model parameterization that is well-suited to inverse techniques and allows us to use the full temporal evolution of the data in the inverse procedure.

[4] Models of volcanic eruptions that include the physics governing magmatic processes [e.g., *Jaupart*, 1996; *Melnik and Sparks*, 1999; *Mastin and Ghiorso*, 2000; *Massol et al*., 2001; *Barmin et al*., 2002; *Costa et al*., 2007] provide valuable insight into various types of eruptive behavior, including cyclic activity. In order to use these models in an inversion, they must relate changes in pressures and tractions in magma to stresses and strains in the host rock in order to predict observations such as ground deformation. *Anderson and Segall* [2011] (hereafter referred to as Part 1) developed a relatively simple numerical, physics-based

Additional supporting information may be found in the online version of this article.

[1]Department of Geophysics, Stanford University, Stanford, California, USA.

[2]Now at: Hawaiian Volcano Observatory, U.S. Geological Survey, Hawaii National Park, Hawaii, USA.

Corresponding author: K. Anderson, Hawaiian Volcano Observatory, U.S. Geological Survey, Hawaii National Park, HI 96718 USA. (kranderson@usgs.gov)

2169-9313/13/10.1002/jgrb.50169

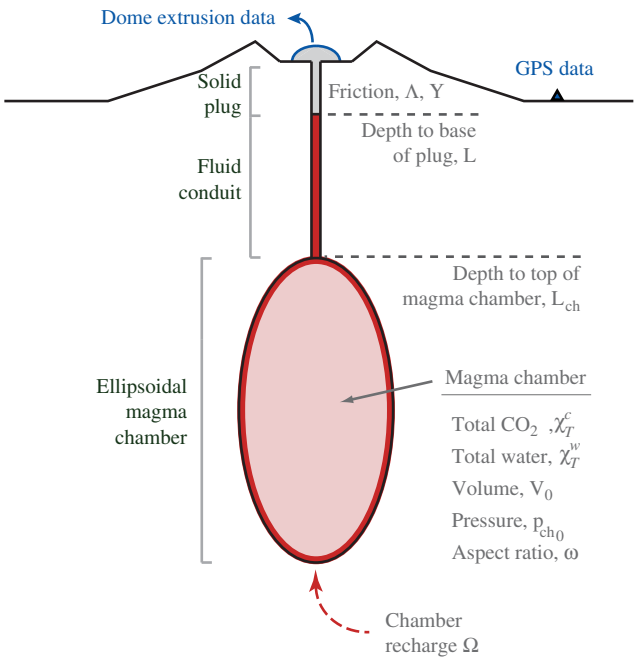

Figure 1. Conceptual model geometry. Pressure in the magma chamber drives flow through the fluid conduit and slip of the solid plug in the upper conduit. Some key model parameters are shown on the right side of the figure. In this study the model is constrained by observations of ground deformation and lava dome extrusion, but other types of data such as CO_2 emissions and gravity could also be considered.

model of an effusively erupting silicic volcano and showed that, with coupling to the host rock, it could be used to predict ground displacement and lava extrusion time series.

[5] To the extent that a model is a reasonable representation of a volcanic system, comparing model predictions with data allows us to infer properties of the volcanic system. Many commonly used inverse techniques are cast as optimization problems, in which the goal is to determine a "best-fitting" set of model parameters which minimizes the misfit between observations and model predictions (usually calculated in a least-squares sense). Such approaches do not attempt to fully characterize the uncertainty associated with model parameters, and as a result, conclusions drawn from them may be inadequate or even misleading (consider, for instance, that very different sets of model parameters may yield very similar fits to the data). This is particularly true when the forward model is highly nonlinear, as is the case for most physics-based models (due in part to complex constitutive laws) or when inverting using diverse data sets.

[6] When inverting using a physics-based model, and when computationally feasible, quantifying as well as possible the full uncertainties associated with estimated model parameters may be a better choice than optimization [e.g., *Sambridge and Mosegaard*, 2002; *Melnik and Sparks*, 2005]. In a Bayesian approach to the inverse problem, probability distributions are used to characterize estimated model parameters as well as any available independent a priori information. (Physics-based models are well-suited for constraint by a priori information; for example, a petrological observation could be used to constrain a model's melt water content.) By comparing model predictions with data and combining with prior information, it is possible to formulate a posterior probability density function (PDF) which characterizes uncertainty in the estimated model parameters, taking into account uncertainty in both the data and a priori information (in this work we do not attempt to account for uncertainty associated with the fact that the forward model must be an imperfect representation of the earth). The posterior PDF may be efficiently characterized using the Markov Chain Monte Carlo (MCMC) algorithm.

[7] In this work we develop a novel technique for using a physics-based forward model with diverse volcanological data sets in a probabilistic inverse procedure. We apply our technique to the 2004–2008 eruption of Mount St. Helens, using wide prior bounds on model parameters (weakly informative prior information) to test the ability of the data to constrain these parameters. We compare results to independent information from petrology, geodesy, and other techniques. We also compare inversions using simple analytical models with those using physics-based models, and inverting different types of data (net GPS displacements, time-dependent geodetic data, and time-dependent geodetic data plus observations of lava dome growth). We are able to demonstrate that the approach described in this work offers a number of important advantages over more traditional techniques, including the remarkable ability to infer melt volatile content using observations of ground displacements and lava dome extrusion, and the ability to estimate magma chamber recharge from a deeper source. The inclusion of additional data sets, such as gravity changes or gas emissions, should in the future provide additional constraints on model parameters, and because the principles outlined in this work are general, with changes to the forward model the technique should be applicable to a wide variety of volcanoes.

2. Physics-Based Forward Model

[8] The forward model is fully parameterized by properties of the volcanic system at the onset of the eruption ($t = 0$). The model consists of an ellipsoidal magma chamber connected to the surface by a cylindrical vertical conduit of constant radius (Figure 1). The chamber is modeled as a lumped parameter with a single time-dependent pressure, corrected for magmastatic pressure gradient to different depths. During an eruption, pressure in excess of the weight of the magma column drives flow out of the chamber and through the conduit towards the surface. Flow of magma in the lower part of the conduit is modeled as Newtonian, with dissolved gas (H_2O and CO_2), exsolved gas, phenocryst, and melt phases. Viscosity of the fluid magma is calculated as a function of dissolved water concentration, temperature, and phenocryst volume fraction, but we do not consider the effect of water exsolution on crystallization. At a constant, specified, solidification depth, the magma crystallizes into a solid plug, the entire length of which slips upward along circumferential faults with a steady-state velocity-dependent friction law. Gas is not lost from the fluid conduit, but is assumed to escape at the fluid/plug interface to increase the density of melt in the upper conduit to the observed plug density (inferred from the density of sampled lava, for instance). Magma may flow into the chamber from a deeper source, recharging it at a rate directly proportional to the

Table 1. Symbols in the System of Equations

Symbol	Description
p, p_p	Pressure (conduit, base of plug)
p_{ch}, p_{cc}, p_{deep}	Pressure (chamber top, chamber center, deep)
V_0	Chamber volume
R	Conduit radius
z	Vertical spatial coordinate
ρ, ρ_{cc}	Bulk magma density (conduit, chamber center)
ρ_α, ρ_c, ρ_λ, ρ_ϕ	Phase density (bubbles, dissolved volatiles, melt, phenocrysts)
ρ_p, ρ_l	Density (solid plug, lithostatic)
L	Length of solid plug
v, v_{p}, v_{ch}	Velocity (magma, plug, chamber exit)
η	Magma viscosity
β_{m}, β_{ch}	Compressibility (magma, chamber)
Ω	Chamber influx coefficient
T	Magma temperature
η, η_χ, η_ϕ	Viscosity (total, from diss. H_2O, from phenocrysts)
p^w, p^c, R^w, R^c	Partial pressures and gas constants (H_2O, CO_2)
m^w, m^c	Mole fraction (H_2O, CO_2)
S^w, S^c	Solubility relationships for H_2O and CO_2
χ_T^w, χ_d^w, χ_e^w	Mass conc. H_2O (total, dissolved, exsolved)
χ_T^c, χ_d^c, χ_e^c	Mass conc. CO_2 (total, dissolved, exsolved)
χ_{d}, χ_{e}	Mass conc. H_2O + CO_2 (dissolved, exsolved)
ϕ	Mass fraction phenocrysts
ϕ^v, α^v, λ^v	Vol. fraction (phenocrysts, exsolved gases, melt)
h	Lava dome height, from observations
v_r, f_0, a	Friction (reference velocity, nominal coefficient, rate-dependence)
Υ, Λ	Grouped friction parameters
σ_c, ζ	Friction coefficients (normal stress, pore-fluid)

difference between a fixed deep pressure and the chamber pressure. The current model does not consider processes such as crystallization or an increase in friction that could terminate an eruption before the pressure drops to magmastatic, so we enforce a cessation at the observed end of the eruption. Chamber recharge in post-eruptive periods may result in repressurization of the magmatic system.

[9] Key model physics are governed by the expressions given below; for a complete description of the model formulation and numerical solution technique, see Part 1. Symbols are defined in Table 1.

$$0 = \frac{\partial p}{\partial z} + \rho g + \frac{8\eta v}{R^2} \tag{1}$$

$$\frac{\partial \rho}{\partial t} = -\frac{\partial}{\partial z}(\rho v) \tag{2}$$

$$\frac{\mathrm{d}p_{\mathrm{ch}}}{\mathrm{d}t} = \frac{\Omega(p_{\mathrm{deep}} - p_{\mathrm{ch}}) - \pi R^2 v_{\mathrm{ch}}}{V_0(\beta_m + \beta_{\mathrm{ch}})} \tag{3}$$

$$\beta_m = \frac{1}{\rho_{\mathrm{cc}}}\frac{\partial \rho_{\mathrm{cc}}}{\partial p_{\mathrm{cc}}}; \quad \beta_{\mathrm{ch}} = \frac{1}{V}\frac{\partial V}{\partial p_{\mathrm{cc}}} \tag{4}$$

$$\rho = \left[\frac{1-\phi}{1+\chi_e+\chi_d}\left(\frac{\chi_e}{\rho_\alpha} + \frac{\chi_d}{\rho_c} + \frac{1}{\rho_\lambda}\right) + \frac{\phi}{\rho_\phi}\right]^{-1} \tag{5}$$

$$\rho_\alpha = p^w/(R^w T) + p^c/(R^c T) \tag{6}$$

$$\eta = \eta_\chi\left(\chi_d^w, T\right)\eta_\phi\left(\phi^v\right) \tag{7}$$

$$\chi_d^w = \chi_T^w - \chi_e^w = S^w(m^w, m^c, p, T) \tag{8a}$$

$$\chi_d^c = \chi_T^c - \chi_e^c = S^c(m^w, m^c, p, T) \tag{8b}$$

$$v_p = 2\Upsilon \sinh\left\{\frac{R[p_p - \rho_p(L+h)g]}{\Lambda \rho_l g L^2}\right\} \tag{9a}$$

$$\Upsilon = v_r/\exp(f_0/a); \quad \Lambda = a\sigma_c(1-\zeta) \tag{9b}$$

[10] Equations (1) and (2) represent conservation of momentum and mass, respectively, for flow in a 1D cylindrical conduit. Equation (3) gives the evolution of chamber pressure with time. Equations (4) are used to compute the compressibility of magma in the chamber and of the chamber itself (the latter is computed numerically as a function of chamber depth, aspect ratio, and host rock shear modulus using the finite element method as described in Part 1). Equation (5) is used to calculate bulk magma density in terms of the melt, phenocryst, and volatile densities, where the gas phase densities are calculated using the ideal gas law in equation (6) and following Part 1. Equation (7) is used to calculate the viscosity of the magma using functions η_χ and η_ϕ given in *Hess and Dingwell* [1996] and *Costa* [2005] (see also: Comments on "viscosity of high crystal content melts: dependence on solid fraction," arXiv:physics/0512173v2), respectively. Equations (8a) and (8b) are used to calculate combined H_2O and CO_2 solubility in the melt using relations S^w and S^c in *Liu et al.* [2005]. Equation (9a) gives the velocity of the solid plug in terms of the pressure acting on its base, and is derived from a force balance acting on the plug combined with a regularized steady-state rate-dependent friction law (see Part 1). Frictional parameters are grouped into Υ and Λ in equations (9b); the former is a scaled reference velocity while the latter is a dimensionless coefficient combining frictional and stress ratio parameters. The normal stress coefficient σ_c relates normal stress on the

fault to lithostatic pressure, and the pore-fluid coefficient ζ is the ratio of pore-fluid pressure to lithostatic pressure.

[11] Observables include extruded rock volume $V_{ex}(t)$ as a function of time, and ground deformation $\mathbf{u}(\mathbf{x}, t)$ as a function of both space and time, calculated using:

$$V_{ex}(t) = \pi R^2 \int_0^t v_p \left(1 - \alpha^v\right) \mathrm{d}t \tag{10}$$

$$\mathbf{u}_i(\mathbf{x}, t) = (u_{\mathrm{cc}})_i + (u_p)_i + (u_\tau)_i; \quad i = x, y, z. \tag{11}$$

[12] Equation (10) is used to calculate dense rock equivalent (DRE) extruded volume, where α^v is the gas volume fraction. Equation (11) is used to calculate surface displacements in directions x, y and z (or for radially symmetric models along vertical and radial coordinates). Functions u_{cc}, u_{p}, and u_τ give displacements due to the evolving chamber pressure, conduit pressures, and conduit shear tractions, respectively, and may be precomputed using numerical methods and arbitrarily complex model geometries, or calculated using simple analytical approximations (computational cost and desired realism must be considered when choosing an approach). For a linearly elastic medium, when chamber depth is large relative to chamber dimensions and one principle axis is vertical, displacements due to the magma chamber may be calculated using the latter approach with

$$\mathbf{u}_i(\mathbf{x}, t) = \frac{V_0 \Delta p_{\mathrm{ch}}(t)}{\mu L_{\mathrm{cc}}^2} f_i(L_{\mathrm{cc}}, \omega, \nu, \mathbf{x}), \tag{12}$$

where $\Delta p_{\mathrm{ch}}(t)$ is the time-evolving pressure change in the magma chamber, μ is the shear modulus of the host rock, ω is the aspect ratio of the chamber, ν is Poisson's ratio, function f_i depends on the model used [e.g., *Segall*, 2010], and L_{cc} is centroid depth calculated geometrically using $L_{\mathrm{cc}} = L_{\mathrm{ch}} + \left(3V_0\omega^2/4\pi\right)^{1/3}$ where L_{ch} is the depth to the top of the chamber. Note that only for finite analytical or numerical source models relatively near the surface will f_i depend on V_0, except through this influence on L_{cc}.

[13] By assuming that all CO_2 originally dissolved in the magma is advected to the surface before venting into the atmosphere [e.g., *Gerlach et al.*, 2008], and neglecting scrubbing of gases by groundwater, CO_2 emissions may be calculated by $\pi R^2 \chi_T^c \rho_\lambda \int_0^t v_p \lambda^v \mathrm{d}t$, but we save a consideration of gas emissions for future work.

3. Bayesian Formulation and Inversion

[14] The data vector $\mathbf{d}$ is a nonlinear function of the model parameters $\mathbf{m} = [m_1, m_2 \ldots, m_M]^{\mathrm{T}}$, plus error ϵ, such that $\mathbf{d} = \mathbf{G}(\mathbf{m}) + \epsilon$. Function $\mathbf{G}$ is the forward model, described in section 2. The data vector includes all observations which can be predicted by $\mathbf{G}$, and may include diverse time-varying data sets (the data sets used in this work are described in section 4, and the data used in different inversions are noted in section 5). In a Bayesian inverse procedure, the probability associated with a given model set of model parameters $\mathbf{m}$ is a function of how well these parameters are able to explain the data given its uncertainties, and also any additional a priori information that may be available.

3.1. Defining the Posterior Probability

[15] The posterior probability density function is calculated using Bayes' Theorem:

$$P(\mathbf{m}|\mathbf{d}) \propto P(\mathbf{d}|\mathbf{m})\, P(\mathbf{m}), \tag{13}$$

where the likelihood function $P(\mathbf{d}|\mathbf{m})$ measures the fit between the model predictions and the observed data and $P(\mathbf{m})$ encodes prior information on the model parameters.

[16] The data vector $\mathbf{d}$ may incorporate K independent data sets, $\mathbf{d} = \left[\mathbf{d}_1^{\mathrm{T}}, \mathbf{d}_2^{\mathrm{T}}, \ldots, \mathbf{d}_K^{\mathrm{T}}\right]^{\mathrm{T}}$, where data sets are independent in the sense that uncertainties between data sets are not correlated. We assume that errors ϵ_k for each data set follow Gaussian distributions with mean $\mathbf{0}$ and covariance Σ_k, so $\epsilon_k \sim N(\mathbf{0}, \Sigma_k)$. The likelihood function for multiple normally distributed independent data sets is the product of the likelihoods of the individual data sets, so

$$P(\mathbf{d}|\mathbf{m}) = \prod_{k=1}^{K} \left\{ (2\pi)^{-N_k/2} \left|\Sigma_k\right|^{-1/2} \exp\left(-\frac{1}{2}\mathbf{r}_k^{\mathrm{T}} \Sigma_k^{-1} \mathbf{r}_k\right) \right\} \tag{14}$$

where $|\Sigma_k|$, N_k, and $\mathbf{r}_k$ are the determinant of the covariance matrix, number of data points, and residual vectors, respectively, associated with the kth data set, and residuals are calculated by $\mathbf{r}_k = \mathbf{d}_k - \mathbf{G}_k(\mathbf{m})$. Note that covariance matrices may be scaled to account for unmodeled error or to control the relative weighting of the different data sets [e.g., *Fukuda and Johnson*, 2008].

[17] Assuming independence, prior probability $P(\mathbf{m})$ is given by the product of the prior probabilities for each of the model parameters n, so that $P(\mathbf{m}) = \prod_{n=1}^{M} P(m_n)$, where M is the total number of model parameters. A simple uniform prior consists of a lower and upper bound on a model parameter. If uniform priors are available on additional dependent quantities calculated during the forward model simulation, which we here refer to as dependent parameters $\tilde{\mathbf{m}}$, they may trivially be applied by setting $P = 0$ when these bounds are not satisfied.

[18] Care must be taken to use the correct homogeneous probability density $\mathcal{H}(m)$ to describe the state of null information about a parameter [*Mosegaard and Tarantola*, 2002]. In particular, for so-called Jeffreys parameters (inherently positive parameters with natural reciprocals, such as a chamber's aspect ratio), the homogeneous probability density is not a constant K but is given instead by $\mathcal{H}(m) = K/m$. This may be understood intuitively by considering an example: in the absence of other information, the aspect ratio of a magma chamber $\omega \in \{0.1 : 1\}$ must be as likely as $\omega \in \{1 : 10\}$, so $\mathcal{H}$ must be uniform on a logarithmic rather than linear (cartesian) scale. Since the logarithm of a Jeffreys parameter is a parameter with a constant homogeneous probability distribution, for simplicity we estimate the logarithms of all Jeffreys parameters.

3.2. Sampling the Posterior Probability With MCMC

[19] Markov Chain Monte Carlo (MCMC) sampling allows for efficient characterization of posterior probability distributions by sampling the model space according to a probability distribution that is as close as possible to the posterior distribution, such that sets of model parameters consistent with both prior information and the fit-to-data are picked more often than incompatible (low-probability) models [*Mosegaard and Tarantola*, 1995]. The Metropolis-Hastings rule [*Metropolis et al.*, 1953; *Hastings*, 1970] is perhaps the most important technique for controlling the random walk such that, after a large number of iterations, the density of samples begins to approximate the posterior probability distribution itself.

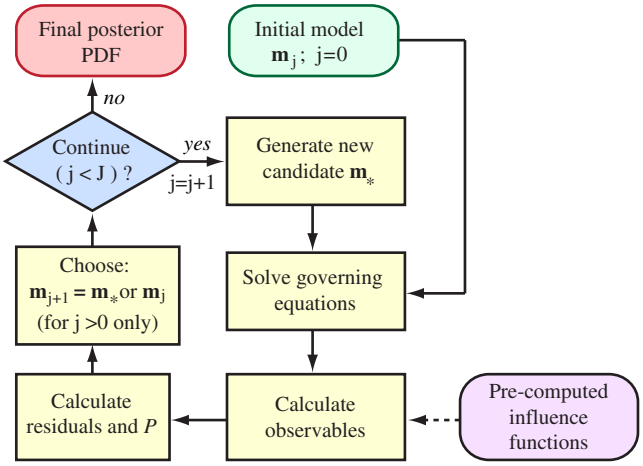

Figure 2. Schematic showing model solution and MCMC iterative procedure described in the text.

[20] In the approach we follow, a set of candidate model parameters $\mathbf{m}_*$ is generated from the current set of model parameters $\mathbf{m}_j$ (subscript j indicates step number) by perturbing each parameter of $\mathbf{m}_j$ by an amount $s_n \Delta m_n$, where s_n is a random number generated from a uniform distribution on the interval [–1, 1] and Δm_n is the random walk step size for the nth parameter. The next set of model parameters $\mathbf{m}_{j+1}$ is then chosen according to

$$\mathbf{m}_{j+1} = \begin{cases} \mathbf{m}_* & \text{if } P(\mathbf{m}_*|\mathbf{d}) / P(\mathbf{m}_j|\mathbf{d}) \geq w_* \\ \mathbf{m}_j & \text{otherwise,} \end{cases} \tag{15}$$

where w_* is a random number generated from a uniform distribution on the interval [0, 1]. Candidate models which improve upon the probability of the current model are always accepted, while candidate models with lower probability may or may not be accepted (allowing the inversion to escape from local minima).

[21] The step size Δm plays an important role in convergence, and can be optimized by calculating the percentage of models accepted; while there is no ideal theoretical value, several studies suggest that <50% acceptance rate is appropriate [*Gamerman and Lopes*, 2006], but very small acceptance rates are not efficient so trial-and-error may be required.

[22] Substituting equations (13) and (14) into the test $P(\mathbf{m}_*|\mathbf{d}) / P(\mathbf{m}_j|\mathbf{d}) \geq w_*$, and taking the logarithm, we obtain the test of acceptance:

$$-\sum_{k=1}^{K} \left[\frac{1}{2} \mathbf{r}_k^{\mathrm{T}} \Sigma_k^{-1} \mathbf{r}_k \right]_* + \ln[P(\mathbf{m}_*)]$$

$$+\sum_{k=1}^{K} \left[\frac{1}{2} \mathbf{r}_k^{\mathrm{T}} \Sigma_k^{-1} \mathbf{r}_k \right]_j - \ln[P(\mathbf{m}_j)] \geq \ln(w_*), \tag{16}$$

where terms with the * subscript correspond to the candidate step and terms with the j subscript correspond to the current step.

[23] If any of the priors $P(\mathbf{m}_*) = 0$, then $\mathbf{m}_*$ is rejected without running the forward model. We also check priors on dependent parameters $\tilde{\mathbf{m}}_*$ after running the forward model. For uniform priors, $P(\mathbf{m})$ is either a constant nonzero value if all priors are satisfied or else 0 if one or more is not, so $\ln[P(\mathbf{m})]$ terms in (16) need not be calculated.

3.3. Iterations

[24] Figure2 shows an outline of the procedure used to estimate posterior PDFs. Beginning with an initial set of model parameters $\mathbf{m}_0$, the governing equations are solved to obtain time-dependent magma pressure, tractions, and other properties. Predicted observations are then calculated using equations (10) and (11), optionally using precomputed influence functions in the computation of ground deformation. Candidate models are accepted or rejected using residuals $\mathbf{r}$ and equation (16), a new candidate model is chosen, and the process is repeated for a total of J iterations. The number of iterations required to adequately characterize the posterior probability distribution depends upon the complexity of the distribution, which in turn depends upon the forward model, number of estimated model parameters, priors, and data. In the inversions detailed in section 5, we used J of order 1–10 million.

[25] Before running an inversion we experiment with different step sizes in a trial-and-error procedure until we obtain acceptance rates of roughly 20% if possible; this step size is then used in the full inversion. To better ensure full coverage of the posterior PDF and to reduce correlation between points, we start different Markov Chains at randomly selected $\mathbf{m}_0$. We terminate iterations when independent Markov Chains begin to yield similar distributions which are no longer substantially changed by further iterations. After termination of the inversion, following standard procedures we remove a "burn-in" period of early MCMC samples from results. The number of samples discarded is chosen by examining the evolution of P with MCMC step, for each independent Markov Chain, and subjectively choosing a burn-in period corresponding to early,

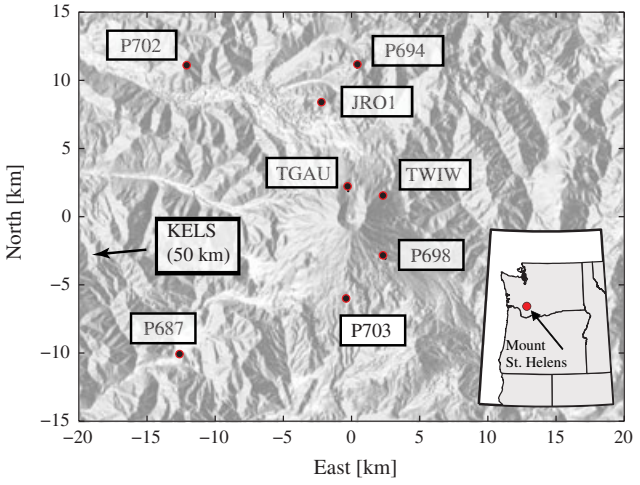

Figure 3. Map of GPS stations in this study, with inset showing location of Mount St. Helens in Washington state. Only post-eruptive data was used from some stations.

very low-P samples. Final PDFs consist of the combination of the independent Markov Chains.

4. Mount St. Helens 2004–2008

[26] The 2004–2008 eruption of Mount St. Helens was characterized by the effusive extrusion of a large dacitic lava dome in the crater formed by the 1980 eruption of the volcano [*Vallance et al.*, 2008; *Scott et al.*, 2008]. Petrologic evidence suggests that the ascending magma reached a semi-solid state at < 1 km depth beneath the crater floor and was forced upwards and out of the conduit along well-developed ring faults [*Cashman et al.*, 2008; *Pallister et al.*, 2008], in processes associated with extensive shallow seismicity [*Moran et al.*, 2008; *Thelen et al.*, 2008]. Although periodic behavior was observed at short time scales in the seismic and tilt data [*Moran et al*., 2008; *Iverson et al*., 2006; *Anderson et al*., 2010], the eruption as a whole was characterized by a steady decline in the rates of dome extrusion and GPS-measured ground deformation.

4.1. Data

[27] In this work we consider lava dome extrusion and GPS data; CO_2 emissions may be considered in future work.

4.1.1. Ground Deformation (GPS)

[28] Precursory deformation was not detected by the Mount St. Helens campaign GPS network nor using radar interferometry in the years preceding the eruption [*Lisowski et al.*, 2008; *Poland and Lu*, 2008]. A dual-frequency continuous GPS station JRO1 was operational prior to the eruption at the Johnston Ridge Observatory ∼9 km north of the volcano (Figure 3), and 11 more continuous GPS stations were installed within the first weeks of the eruption.

[29] We obtained daily GPS solutions from the Pacific Northwest Geodetic Array (PANGA) and removed non-volcanic deformation by correcting for seasonal effects, rigid-block rotation and uniform strain accumulation caused by convergence of the Juan de Fuca plate [e.g., *Lisowski et al*., 2008; *Palano et al*., 2012], and episodic slip events. GPS processing and noise estimation is described in section S1 of the supporting information; note that our approach here differs somewhat from that in Part 1.

[30] Clear volcanic deformation was not detected at station JRO1 prior to late September 2004, although results are somewhat ambiguous due to uncertainty in removing tectonic deformation (section S1). Volcanic deformation was detected at JRO1 at approximately the same time as the first seismic swarm, when the station began to move downward and radially inward towards the volcano consistent with the deflation of a mid-crustal magma reservoir (see Figure 4 and *Lisowski et al*. [2008]). Deformation during the vent-clearing phase of the eruption (roughly the first 2–3 weeks) was rapid, at about 0.5 mm/day of inward motion, but slowed significantly (Figure 4b) after an explosion on 5 October [*Lisowski et al.*, 2008].

[31] Post-eruptive deformation from January 2008 to the present has been characterized on a broad scale by outward motion of most stations away from the volcano (Figure 4) [*Lisowski and Battaglia*, 2011; *Palano et al.*, 2012]. Inward displacements observed at high-elevation stations are not detected in the stations used in this study [*Lisowski and Battaglia*, 2011].

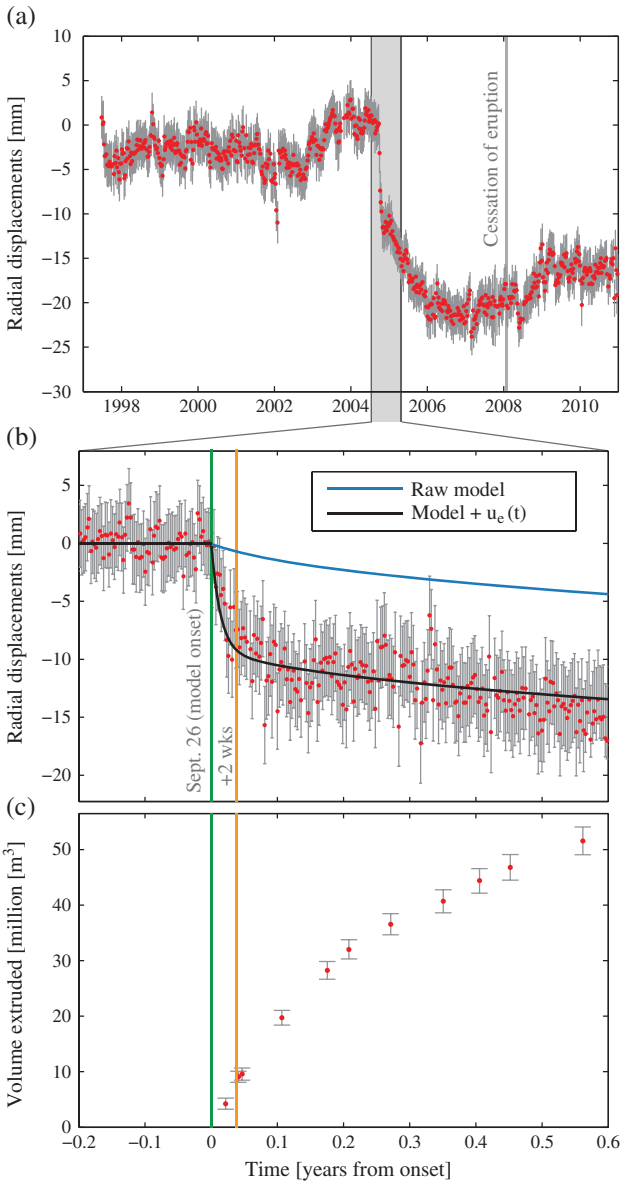

Figure 4. (a) Weekly radial-from-the-vent GPS time series at JRO1 after removing tectonic motion (see section S1 of the supporting information). At the onset of the eruption in late 2004, the station moved rapidly inward towards the vent. Outward motion resumed at, or somewhat before, the cessation of the eruption. Error bars are 1σ, white noise only. (b) Rapid deformation was observed during the first 2 weeks of the eruption and a significantly reduced rate of deformation thereafter. The blue line shows model predictions if the vent-clearing phase is not modeled separately, while the black line shows the effect of the added vent-clearing term. (c) Only one dome volume observation is available from the vent-clearing phase of the eruption.

4.1.2. Dome Volume and Height

[32] *Schilling et al.* [2008] estimated the volume of extruded lava using photogrammetry. A ∼10 million m^3 welt grew on the surface of the crater glacier prior to new lava first appearing on the surface on 11 October 2004 [*Vallance et al.*, 2008]. We take the volume of the welt to be equal to

subglacial extrusion and add it to subsequent estimates of extruded volume in order to calculate total extruded volume V_{ex}, calculating dense-rock-equivalent (DRE) volumes using an estimated dome porosity of 10% [*Gerlach et al.*, 2008]. Estimated uncertainties in individual volume measurements are roughly ±4% [*Schilling et al.*, 2008]. We also include an uncertainty of 1 million m^3 for the welt volume (about 10% of the estimate of pre-4-October extrusion beneath the glacier) and propagate this error to all subsequent volumes. Lava extrusion volumes from early in the eruption are shown in Figure 4c.

[33] We use estimates of lava dome height above the vent from *Mastin et al.* [2008] and the Cascades Volcano Observatory. Dome heights are referenced to the elevation of the glacier surface at approximately 2100 m above sea level (subglacial growth of the dome could not be observed, but changes in back pressure associated with displacement of 100 m or more [*Vallance et al.*, 2008] of glacial ice would have resulted in a smaller change in back pressure on the vent than subaerial growth). Dome height grew rapidly early in the eruption and then fluctuated at roughly 200 m (Figure S6).

4.2. Specialization of Forward Model for MSH

[34] The implicit model assumption of a continuous magma reservoir, rather than, for instance, a plexus of dikes and sills, is supported at MSH by petrologic evidence of large-scale convection of amphiboles [*Rutherford and Devine*, 2008], thermo-mechanical processes which would make a highly irregular chamber unlikely [*Gudmundsson*, 2012] (assuming the chamber at MSH persists between eruptions), and possibly by seismic tomography [*Waite and Moran*, 2009]. A sill-like magma chamber is not generally consistent with GPS observations which favor a vertically elongate source [*Lisowski et al.*, 2008]. The presence of a narrow, vertical, cylindrical conduit between the chamber and surface is supported by earthquake hypocentral locations [*Musumeci et al.*, 2002]. The radial symmetry of the model is consistent with generally radial GPS displacements during the eruption.

[35] The assumption of steady-state velocity-strengthening friction on the boundary between the plug and conduit is consistent with the observation of steady, slowly declining, non-oscillatory eruptive behavior, and is probably necessary in order for an eruption to be sustained as pressure in the chamber drops. (Drumbeat earthquakes [*Iverson et al*., 2006; *Moran et al*., 2008] do suggest that rate-weakening behavior probably did occur on small fault patches, although an alternative explanation for these events involves an opening and closing steam- or fluid-filled crack [*Waite et al.*, 2008].)

[36] Ring-shear tests on extruded fault gouge at MSH from early 2005 suggest the possibility of both rate-weakening and rate-strengthening behavior [*Moore et al.*, 2008], but at experimental temperatures far below the in situ conditions at MSH (higher temperatures, associated with the transition to crystal plasticity, favor rate-strengthening behavior [*Blanpied et al.*, 1995; *Scholz*, 1998], as does the presence of fault gouge, which is abundant at MSH). Peak strength was observed to increase logarithmically with time of static contact for MSH dome rocks [*Moore et al.*, 2008], but for simplicity we assume steady-state friction (steady state is achieved after a displacement of order d_c, and laboratory data suggest that d_c is small enough that the steady-state assumption could only be violated at the very earliest phase of the eruption).

[37] The onset of GPS-recorded deformation at MSH was approximately coincident with the onset of seismic activity on 23 September [*Lisowski et al.*, 2008; *Moran et al.*, 2008], and with the first evidence of extrusion (new crevassing and uplift in the glacier) which was observed on 26 September [*Dzurisin et al.*, 2008]. We take 26 September as the date of eruption onset ($t = 0$).

[38] The vent-clearing phase of the eruption included higher levels of seismicity, several phreatic explosions (the last of which was associated with a large decrease in RSAM) [*Moran et al.*, 2008], and extrusion of lava beneath the glacier rather than onto the surface. As noted, these processes were associated with very high rates of deformation at the single available continuous GPS station (JRO1), but the extrusion data lack the temporal resolution to determine if the vent-clearing phase of the eruption was also associated with anomalously high rates of extrusion (Figure 4c). If rapid motion occurred at JRO1 without high rates of extrusion, the implication is that a volume loss in the deep magma chamber was compensated not by extrusion but by a volume increase somewhere else in the system, such as at shallow depths to which JRO1 would have been insensitive. Gas loss could also have conceivably reduced magma chamber pressure independently of lava extrusion.

[39] While it would be best to have a physical model for "vent-clearing" processes, observations are inadequate to constrain such a model, and are not accounted for in the forward model used in this study. Failure to account for this high "model uncertainty" during the early eruption biases the data fit for the entire eruption, since later points depend on earlier points (Figure 4b). In the absence of a physical understanding for this phase, we add a term $u_e = u_e(t)$ to equation (11) to account for the vent-clearing phase of the eruption. We find that $u_e(t) = C\exp\left(-t/t_c^u\right)$ with time constant $t_c = 5$ days and amplitude C, obtained with a least-squares fit between GPS data and model predictions for the 14 days immediately following the vent-clearing phase, fits the vent-clearing GPS data well without influencing later observations. With this approach, vent-clearing GPS time series at JRO1 are always well-fit, and early model uncertainty does not propagate into later parts of the time series (Figure 4b).

[40] We model vertical and radial-to-the-vent GPS time series (tangential motions cannot be predicted by the radially symmetric model used in this study so are not analyzed here). We model the data from seven cGPS stations (Figure 3), excluding stations above ~2000 m which experienced significant transients associated with seasonal processes [*Lisowski et al.*, 2008; *Palano et al.*, 2012]. Daily position solutions are averaged to produce weekly time series. To compare observed and predicted displacements, a constant offset is computed by least squares and subtracted from the GPS time series. This technique is applied separately to syn- and post-eruptive periods so that mismodeling syn-eruptive data does not bias post-eruptive residuals. These offsets are calculated for each set of model

Table 2. Partial List of Model Parameters (Fixed, Estimated, and Post-Processed)[g]

K	A	P	Symbol	Description	Fixed Value or Bounds
				Estimated parameters	
✓	✓	✓	V_0	Chamber volume	$\{1 : 200\}$ km^3
✓	✓	✓	ω	Chamber aspect ratio	$\{1 : 10\}$
✓	✓	✓	L_{ch}	Chamber top depth	$\{2 : 12\}$ km
✓			Δp_{ch}	Chamber pressure change	$\{-50 : -1\}$ MPa [a]
	✓		p^x_{ch}	Initial chamber overpressure, above magmastatic	$\{1 : 50\}$ MPa [a]
		✓	p_{ch_0}	Initial pressure at top of chamber	$\{40 : 180\}$ MPa
	✓		$\tilde{\beta}$	System compressibility	$\{10^{-13} : 10^{-8}\}$ Pa^{-1}
	✓		$\tilde{c}$	Conduit conductivity	$\{10^{-5} : 10^{3}\}$ m^4/Pa s
		✓	L	Length of solid plug	$\{500 : 1500\}$ m
		✓	χ^w_T	Mass concentration total water	$\{3 : 9\}$ wt%
		✓	χ^c_T	Mass concentration total carbon dioxide	$\{0 : 4000\}$ ppm
		✓	Ω	Chamber influx coefficient	$\{0.1 : 30000\}$ m^3 day^{-1} MPa^{-1}
		✓	Λ	Friction: $a\sigma_c(1-\zeta)$	$\{0 : 0.05\}$ [b]
		✓	Υ	Friction: $v_r/\exp(f_0/a)$	$\{10^{-6} : 4\times10^{-3}\}$ m/s [b]
				Fixed parameters (partial list)	
✓	✓	✓	μ	Half-space shear modulus	20 GPa
		✓	R	Conduit radius	50 m [c]
		✓	ϕ_{ch}	Mass fraction phenocrysts in chamber	45% [d]
		✓	T	Temperature of melt	1120 K (850° C) [e]
		✓	ρ_p	Density of plug	2000 kg/m^3 [f]
				Dependent parameters and constraints (partial list)	
✓	✓	✓	$V_0\Delta p_{\mathrm{ch}}$	Geodetic source strength	-
✓	✓	✓	ΔV	Volume change in chamber during eruption	-
✓	✓	✓	L_{cc}	Depth of chamber centroid	-
		✓	χ^w_d	Dissolved water concentration	-
		✓	p^{xl}_p	Pressure at base of plug above lithostatic	$\{0 : 15\}$ MPa

[a][e.g., *Mastin et al*., 2009].
[b]see Appendix A.
[c][*Scandone and Malone*, 1985; *Carey and Sigurdsson*, 1985; *Pallister et al*., 2008].
[d][*Pallister et al*., 2008].
[e][*Rutherford and Devine*, 2008].
[f][*Iverson et al*., 2006].
[g]The kinematic GPS inversion uses parameters indicated by a check mark (✓) in the column labeled K; the deflating chamber model uses parameters indicated by a check mark (✓) in the column labeled A, and likewise for the physics-based model in the column labeled P. Not all fixed or post-processed parameters are listed for the physics-based model (see part 1 for a complete list). Bounds for most parameters were chosen to comfortably include independent estimates, when available.

parameters (MCMC iteration). Note also that when calculating residuals we treat syn- and post-eruptive data separately and "reset" the random walk error to zero at the end of the eruption.

[41] Ground deformation generated by the magma chamber is calculated using an approximate solution to the problem of a finite, dipping prolate spheroid subject to constant pressure in an elastic half-space [*Yang et al.*, 1988]. For the relatively deep chamber at Mount St. Helens it behaves as equation (12). Although a modest deviation from radial symmetry in the GPS displacements suggests that the magma chamber may dip slightly from the vertical [*Lisowski et al.*, 2008; *Palano et al.*, 2012], for simplicity we assume a vertical orientation. Deformation generated by the conduit and plug are disregarded (equation (11)), as they are insignificant at the distances of modeled GPS stations from the vent at MSH. We include a first-order correction for topography using station elevations. Zero elevation is fixed to the top of the conduit (the crater floor), and we fix the top of the chamber to lie directly beneath the 1980s eruptive vent.

[42] For simplicity, we set $p_{\mathrm{deep}} = p_{\mathrm{ch}}$ for pre-eruptive times such that chamber pressure is constant before the eruption.

[43] Time-evolving lava dome heights (h in equation (9a)) are derived from fitting observations with a smooth function of the form $h(t) = h_{\max}[1 - \exp(-t/t_c)]$ where $h_{\max} = 220$ and $t_c = 0.09$ (Figure S6a); using a smooth function speeds numerical solution but still captures the essential behavior of extrusion (Figure S6b). Ignoring the growing dome results in significantly over-estimating the extruded volume (Figure S6b).

[44] Non-estimated parameter values are taken from *Anderson and Segall* [2011] unless otherwise noted. For a shallow edifice density (ρ_l in equation (9a), which influences normal stress on the plug), we use 2150 kg/m^3 [*Williams et al.*, 1987].

5. Inversions

[45] For comparison, we begin with an inversion based on a simple kinematic forward model and net GPS displacements and proceed to more complex physics-based models

which predict additional data sets. Key model parameters (Table 2) include magma chamber volume, initial pressure, aspect ratio, and depth; water and carbon dioxide concentration; plug length; magma chamber influx coefficient; and frictional parameters (note that many of these parameters do not apply to the simpler models). Dependent parameters include chamber centroid depth, volume change, and source strength.

[46] For all inversions we use uniform priors on model parameters (Table 2), and in some cases apply additional constraints on dependent parameters. We estimate the logarithm of Jeffreys parameters such as chamber volume, chamber pressure, and aspect ratio. Prior bounds are generally chosen to widely encompass independent estimates from the literature and so that they do not strongly restrict posterior distributions; in this way, we are able to better characterize the ability of the data alone to constrain distributions. Independent constraints on MSH parameters are discussed in section 6.1, and see Appendix A for a discussion of prior bounds on frictional parameters. We find that weighting GPS and extrusion time series by their respective uncertainties yields reasonable results (i.e., both data sets contribute importantly to the posterior PDFs) so additional scaling factors are not required. Note that we also do not attempt to characterize uncertainty in the forward model **G**.

[47] We display posterior PDFs as a grid, with diagonals showing histograms of marginal distributions for individual parameters and off-diagonals showing contoured joint distributions between pairs of parameters; box edges correspond to a priori bounds except where noted (for clarity, note that some dependent parameters use different bounds in different plots). To reduce correlations we plot only every 10th point chosen by the MCMC algorithm for each model parameter. These plots must be interpreted carefully. Note in particular that peaks in histograms (the most frequently sampled values) do not necessarily correspond to best-fitting models, because distributions can be controlled by correlations between parameters even in the absence of constraint by the data.

[48] Note that with the more complex models there are many correlations between parameters and these correlations are not always immediately intuitive. For example, for a fixed chamber top depth, chamber aspect ratio influences the depth of the chamber centroid, which influences the pressure and thus the compressibility of the melt. We will not attempt to detail all the parameter-to-parameter correlations in the posterior distributions which follow, but instead highlight key results.

5.1. Kinematic Ellipsoidal Magma Chamber

[49] We first invert net syn-eruptive radial and vertical GPS displacements at seven stations using the kinematic *Yang et al.* [1988] model of an ellipsoidal magma chamber (equation (12) with $t = t_f$), estimating chamber volume, pressure change, conduit length (depth to top of chamber), and aspect ratio. This approach is typical of that used when inverting GPS data to estimate source geometry and strength. At Mount St. Helens, initial chamber overpressure (above magmastatic) was likely greater than ∼6 MPa based on the height obtained by the lava dome and less than ∼20 MPa based on the strength of the host rock around the chamber [*Mastin et al.*, 2009]. To be conservative, we limit overpressure to 1–50 MPa. Other bounds are shown in Table 2.

[50] The fit to the data (Figure 5a) is good for more distant stations but relatively poor for closer stations which exhibited significant 'wander' (apparently non-volcanic radial and tangential motion) during the eruption. Joint posterior distributions are shown in Figure 5b. Chamber volume and pressure change are not independently resolved (Figure 5b, box 1) but the data are able to constrain their product (equation (12) and *McTigue* [1987]), which when scaled by chamber compressibility yields volume change (box 2):

$$\Delta V = \beta_{\mathrm{ch}} V_0 \Delta p_{\mathrm{ch}}. \tag{17}$$

Volume change ΔV and the product $V_0 \Delta p_{\mathrm{ch}}$ can be thought of as geodetic "source strengths" and can typically be resolved in inversions using kinematic forward models, as here. Note that individual distributions for volume and pressure change are limited by prior constraints on the other parameter (for example, the upper bound on pressure change limits small chamber volumes).

[51] Chamber aspect ratio should in principle be constrained by the ratio of observed vertical to horizontal displacements, and chamber centroid depth by the rate that deformation decays with distance from the source, but these parameters are not resolved here due to wander in the GPS time series (the distribution for centroid depth in box 3 is controlled not by the data but by prior bounds on the parameters from which it is calculated: top depth, aspect ratio, and volume). Chamber top depth (conduit length) is also largely unconstrained.

[52] Although outside the scope of this work, by adding more stations (including campaign GPS sites) we could better resolve the source depth, volume change, and aspect ratio, as in *Lisowski et al.* [2008] and *Palano et al.* [2012]. Also, for consistency with other inversions we calculate net displacements using all syn-eruptive data (exclusive of vent-clearing), but a significantly better signal-to-noise ratio can be obtained using only the first ∼ 1 year of data [*Palano et al.*, 2012], which includes most of the deformation signal and less accumulated random walk (and other) error. We find that inversions using only the first year of data are able to provide significantly better constraint on most model parameters.

5.2. Deflating Elastic Chamber

[53] Quasi-exponential declines in extrusion rate, and sometimes ground deformation, have been interpreted using simple models of a deflating magma chamber in an elastic crust driving Newtonian flow through a conduit [*Wadge*, 1981; *Stasiuk et al.*, 1993; *Segall et al.*, 2001; *Huppert and Woods*, 2002; *Woods and Huppert*, 2003; *Mastin et al.*, 2008]. These models approximate magma as a Newtonian fluid with time- and depth-independent viscosity $\bar{\eta}$ and density $\bar{\rho}$ and lack a frictional plug within the upper conduit (although a solid plug surrounded by a Newtonian fluid between the plug and conduit wall can also be modeled with these expressions [*Mastin et al.*, 2008]), but they move beyond kinematic forward models by allowing both deformation and extrusion data, as well as the time evolution of these observations, to be used to constrain model parameters.

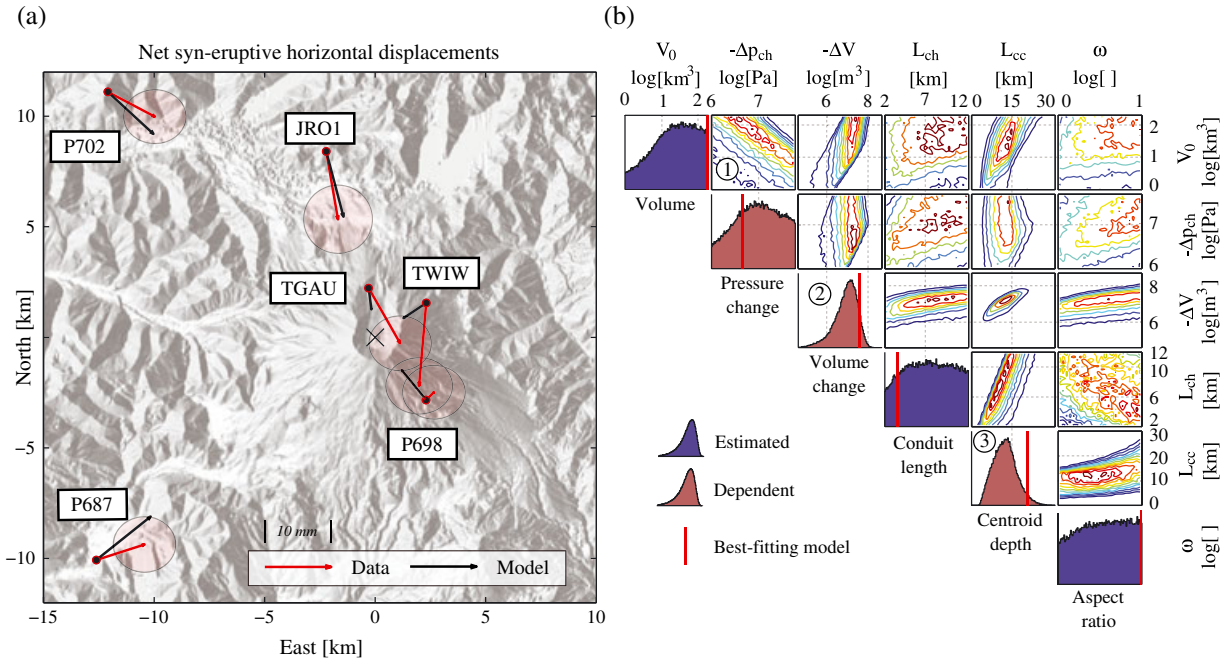

Figure 5. Results from inversion of net GPS displacements using the kinematic *Yang et al.* [1988] model. (a) Data (red) and predictions (black) from best-fitting model, with 1σ confidence ellipses. Station KELS and vertical displacements are also used in the inversion, but not shown. (b) Marginal posterior distributions for estimated parameters are shown on the diagonals in blue and dependent parameters (calculated from estimated parameters) in red (pressure change Δp_{ch} is the negative of the initial overpressure, for which we invert). Vertical red lines indicate parameter values for the best-fitting model. Circled numbers are described in the text. Several parameters are plotted on base-10 logarithmic scales. Plot limits for estimated parameters correspond to a priori values; plot limits for ΔV are calculated from prior limits on terms in $\beta_{ch} V_0 \Delta p_{ch}$ (equation (17)).

[54] As shown in Part 1 (and see references therein), the temporal evolution of syn-eruptive pressure change in the magma chamber, with no chamber influx, is given by

$$\Delta p_{ch}(t) = -p^x_{ch}\left(1 - e^{-t/t_c}\right), \tag{18}$$

and extruded volume by

$$V_{ex}(t) = V_0 \bar{\beta} p^x_{ch}\left(1 - e^{-t/t_c}\right), \tag{19}$$

where the time constant t_c is given by

$$t_c = V_0 \bar{\beta}/c, \tag{20}$$

and does not directly depend on magma chamber pressure. In these expressions, $p^x_{ch} = p_{ch_0} - \bar{\rho} g L_{ch}$ is excess pressure at the top of the chamber above magmastatic at $t = 0$, $\bar{\beta} = \beta_m + \beta_{ch}$ is the total system compressibility, and conduit conductivity $c = \pi R^4/8\bar{\eta}L_{ch}$ for Newtonian flow in a cylindrical conduit. If the chamber pressure decreases to magmastatic during the eruption then initial excess pressure is equal in magnitude to the total pressure change over the entire eruption $\left(\Delta p_{ch} = -p^x_{ch}\right)$, but this will not be true if the eruption is terminated early by the forced cessation we employ in this study. Finally, combining equations (12) and (18) yields predicted displacements:

$$\mathbf{u}_i(\mathbf{x}, t) = -\frac{V_0 p^x_{ch}}{\mu L^2_{cc}} f_i(L_{cc}, \omega, \nu, \mathbf{x})\left(1 - e^{-t/t_c}\right). \tag{21}$$

[55] The system is parameterized as in the previous inversion, but with the addition of conduit conductivity and system compressibility (six unknowns; see Table 2). Note that because conduit length is an independent model parameter, we estimate not c but $\tilde{c} = cL_{ch} = \pi R^4/8\bar{\eta}$, which we will continue to refer to as conduit conductivity. Prior bounds are set as previously, and bounds for new parameters are set based on experience to encompass observed posterior distributions.

5.2.1. Inversion of GPS Data

[56] For comparison with results from the kinematic forward model, and because extrusion data are often not available (or the volcano is not erupting), we first invert using only GPS data. In this case only equations (20) and (21) can be used to relate observations to model parameters. We estimate the ratio $\bar{\beta}/\tilde{c}$ since these parameters appear only together and cannot be uniquely constrained. Because the inversion uses the full time-evolving GPS time series, constraint is provided on the predicted evolution of chamber pressure and thus on the quantity $V_0\bar{\beta}/c$ (equation (20)). However, although chamber volume appears in equation (20) independently of pressure change, it cannot be uniquely resolved without constraint on $\bar{\beta}/\tilde{c}$.

[57] The fit to GPS data is reasonable given the wander in the time series (Figure 6). Posterior distributions (Figure7b) are improved due to the information provided by the time constant; also, due to the accumulation of correlated errors in the data, inversions using the full time series

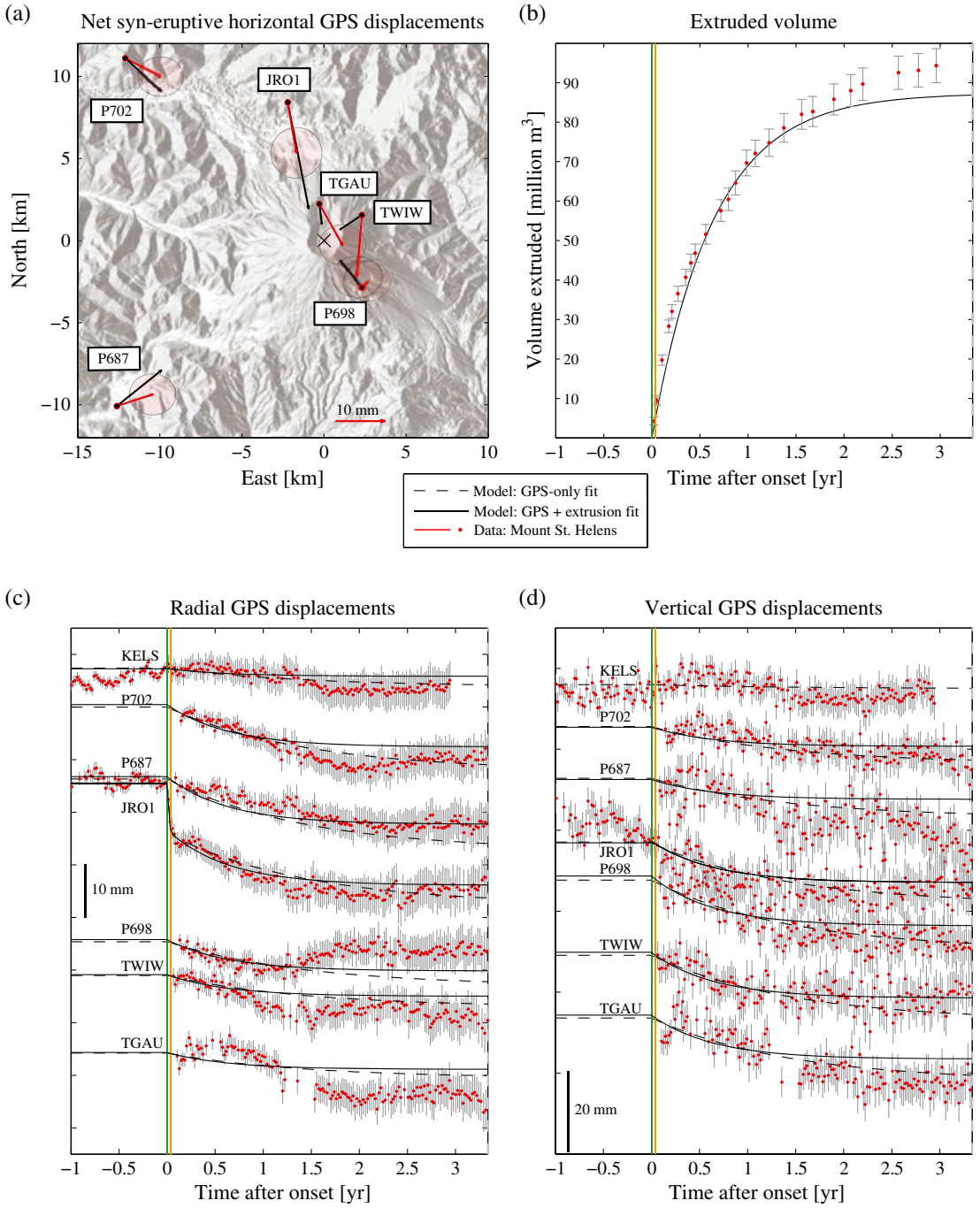

Figure 6. Fit-to-data for deflating elastic chamber model. (a) Net horizontal displacement vectors (for comparison only; inversions use the full time series). Starting positions for each station are calculated at either the beginning of GPS data or the end of the vent-clearing phase of the eruption, whichever came first, and ending positions are calculated at the end of the eruption or end of GPS data, whichever came last. Displacements therefore cover nearly—but not exactly—equivalent time periods at each station. (b) Extrusion time series. The vertical green line shows the onset of the eruption and the amber line shows the end of the vent-clearing phase. (c, d) Radial and vertical GPS displacements. Results from inverting GPS data only are shown with dashed black lines; results using both GPS and extrusion data are shown with solid black lines.

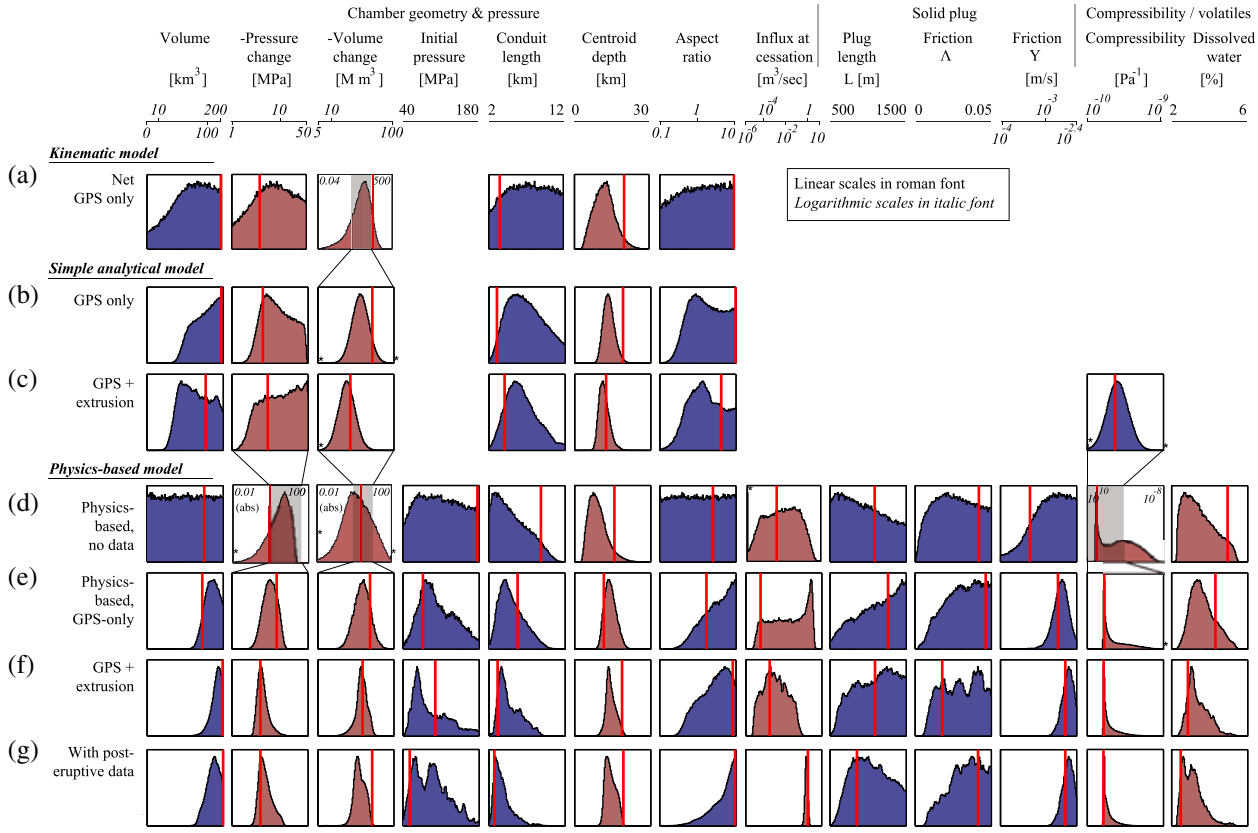

Figure 7. Marginal posterior distributions for parameters estimated in six different inversions. Estimated and dependent parameters are shown with blue and red histograms, respectively. Some histograms have different bounds, as indicated. The text "(abs)" indicates that an absolute value was taken before plotting. Chamber influx is calculated from the chamber influx coefficient and taken at the end of the eruption. Volume and pressure changes in (g) are for the syn-eruptive period only. The asterisk indicates that some values exceed the limits of the plot.

naturally downweight later data, which exhibited considerable wander after the first year of more rapid displacements (Figure S4).

[58] The tighter constraint on source strength results in better estimates for many other parameters. This is evident by comparing joint distributions in Figure S7 to joint distributions from the kinematic inversion in Figure 5b, which exhibit considerably more "smear." Box 1 in both figures shows the improved constraint on source strength (width of the joint distribution), which in combination with prior bounds on these parameters results in tighter distributions for both. Note also the intuitive correlation between volume change and centroid depth in Figure S7, box 2, and compare to the corresponding box in Figure 5b, which shows how limiting source strength improves the estimate of centroid depth.

5.2.2. Inversion of GPS and Extrusion Data

[59] Observations of extruded volume V_{ex} provide another estimate of the time constant (equation (20)), and in addition to previously estimated quantities, make it possible to estimate $V_0\bar{\beta}p^x_{ch}$ from equation (19). Since $\bar{\beta}$ appears separately from $\tilde{c}$ in equation (19), we can estimate these parameters separately (yielding six unknowns). Dividing equation (19) by equation (18) and rearranging, $\bar{\beta} = -V_{ex}/V_0\Delta p_{ch}$. Combining with equation (17) alternatively yields $\bar{\beta} = -V_{ex}\beta_{ch}/\Delta V$ [e.g., *Mastin et al.*, 2008]. Finally, taking the former expression and combining with equation (12) yields

$$\bar{\beta} = -\frac{V_{ex}}{\mathbf{u}_i(\mathbf{x},t)}\frac{f_i(L_{cc},\omega,\nu,\mathbf{x})}{\mu L_{cc}^2}, \tag{22}$$

or $\bar{\beta} \propto V_{ex}/\mathbf{u}$ [*Segall*, 2013]. To the extent that chamber geometry and rock rigidity may be estimated or constrained by the data, observations of extruded volume and ground displacements therefore yield estimates of system compressibility.

[60] Data and the best-fitting model are shown in Figure 6. The fit to extrusion data is reasonable but imperfect, with an under-fit of observations near the end of the eruption. With additional constraint by extrusion data the best-fitting GPS displacements are smaller than in the GPS-only inversion, but still fit the data reasonably.

[61] As expected from theoretical arguments, the data are able to constrain compressibility $\bar{\beta}$ (Figures 7c and 8, box 1). The constraint on compressibility, along with a better estimate of the time constant (at MSH, the time constant derived from the extrusion data is far better constrained than that obtained from the GPS data due to wander in the latter), helps to limit a number of other distributions. Improved

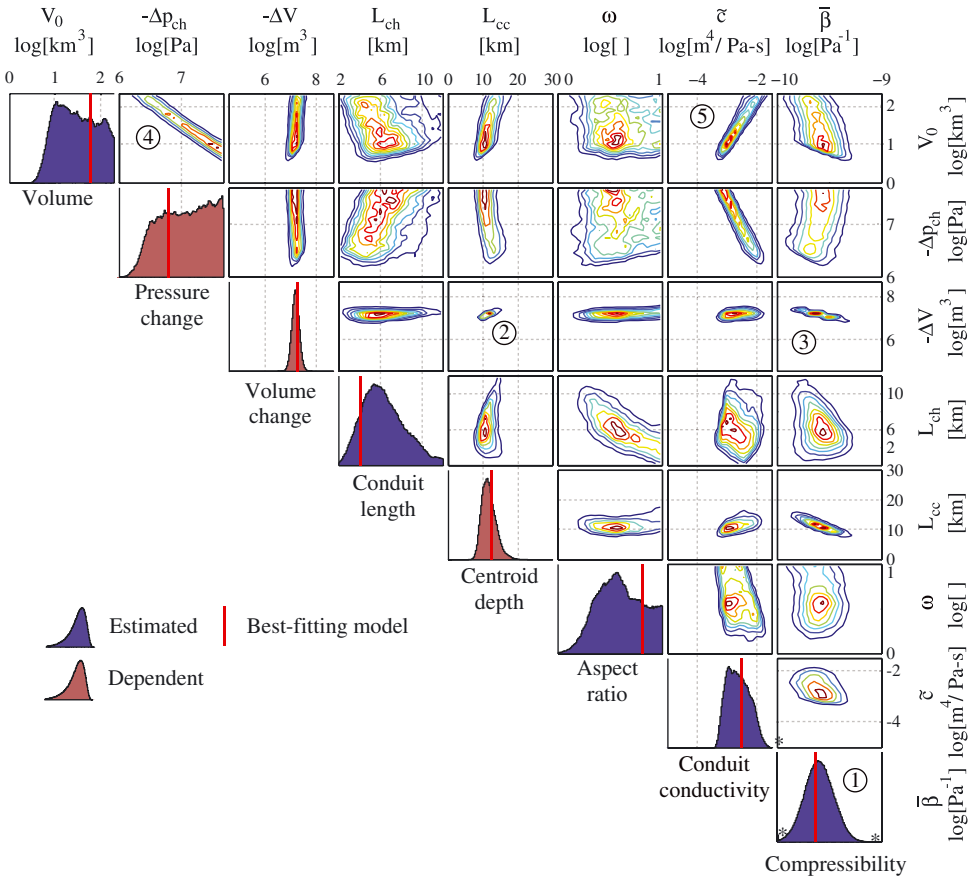

Figure 8. Posterior distributions derived from inversion of GPS and extrusion data using a simple model of a deflating elastic magma chamber. Layout of figure is the same as that in Figure 5b.

constraint on volume change can be understood from the expression $\bar{\beta} = -V_{ex}\beta_{ch}/\Delta V$ above; since V_{ex} is an observation and β_{ch} is only a relatively weak function of estimated model parameters (see Part 1), constraint on $\bar{\beta}$ improves constraint on ΔV. Because deeper chambers must have a larger volume change to fit the geodetic data, the estimate of L_{cc} is also more tightly constrained (note the strong correlations between volume change, centroid depth, and compressibility in boxes 2 and 3 in Figure 8). Chamber volume and pressure change remain highly correlated (box 4), although volume is smaller and pressure change somewhat larger than in the previous inversion. A lower bound on conduit conductivity is also provided by the prior constraint on chamber volume (both influence the time constant in equation (20) and their correlation is evident in box 5).

5.3. Physics-Based Model

[62] The physics-based forward model used in this study is much more computationally expensive than simple kinematic forward models and also has many more parameters (Table 2). To reduce the computational expense of inversions, we fix a number of parameters using independent information. We also do not attempt to separately estimate all frictional parameters, but rather estimate grouped parameters Υ and Λ; see Appendix A. Other new estimated parameters include initial chamber pressure, chamber influx coefficient, plug length, and total water and carbon dioxide content.

[63] We constrain excess conduit pressure above lithostatic at the base of the plug so that the tensile strength of the surrounding rock is not exceeded. The tensile strength of rocks in the shallow crust is unlikely to exceed 10 MPa [e.g., *Sparks*, 1997; *Green et al.*, 2006], and since tensile stress induced by a pressurized conduit is roughly equal to the excess conduit pressure [*Timoshenko and Goodier*, 1970], this suggests a limit of ~10 MPa above lithostatic in the conduit. To be conservative, we constrain $0 < p_p^{xl} < p_{litho} + 15$ MPa. We also reject models with implausibly high or low initial volumetric flow rates (200 m^3/sec and 0.1 m^3/sec, respectively).

5.3.1. Influence of Prior Constraints

[64] The forward model encodes many complex relationships between parameters, and additional relationships are used in the calculation of dependent parameters. Because of this, placing a prior constraint on one parameter (whether estimated or dependent) may influence other parameters in complex ways. To independently evaluate the influence of the prior constraints on the posterior PDFs, we assume that the likelihood function $P(\mathbf{d}|\mathbf{m})$ is constant (that is, the data cannot resolve changes in model parameters), so that $P(\mathbf{m}|\mathbf{d}) \propto P(\mathbf{m})$ (see equation (13)). By performing an 'inversion' for $P(\mathbf{m}|\mathbf{d})$, we are thus able to generate posterior distributions due to the influence of the prior constraints, without the influence of the data.

[65] Results are shown in Figures 7d and S8. Model parameters (blue histograms) are mostly uniform between

prior bounds because they are unconstrained by data, but chamber pressure, conduit length, total water (weakly), and parameters related to the plug resistive force (length and frictional parameters) are non-uniform. These distributions are limited by the a priori constraint on excess pressure at the base of the plug (note for example the correlation in Figure S8, box 1) and initial conduit velocity, as well as physical constraints implied by the governing conservation equations.

[66] Dependent parameters (red histograms) are mostly non-uniform due to prior constraints and/or non-uniformity in parameters from which they are calculated. Centroid depth is controlled geometrically by prior bounds on volume, aspect ratio, and conduit length. A peak at zero exsolved water (Figure S8, box 2) is associated with models that are undersaturated in volatiles, which occurs for any set of model parameters in which chamber pressure is relatively high and total water relatively low. This also corresponds to a peak in compressibility at $\sim 1.7\times10^{-10}$ Pa^{-1}, the compressibility of the system with no exsolved water (due mainly to fixed phenocryst and melt compressibilities, and the nearly constant chamber compressibility). Fixed a priori values for the compressibility of the various phases therefore places a lower limit on system compressibility which is not present in the bulk compressibility estimated using the analytical model (Figure 7c).

[67] Results demonstrate how a physics-based model allows us to constrain many posterior distributions, even without data, by merely placing plausible a priori bounds on certain model parameters, or by constraining certain properties of the model on physical grounds.

5.3.2. Inversion of GPS Data

[68] Inversions using GPS data are able to fit observations reasonably well given the noise in the time series, while predicted extrusion (which does not contribute to the residual in the inversion) is very poor and indicates that best-fitting time constants from GPS and extrusion data are different (Figure 9).

[69] Marginal posterior distributions are shown in Figures 7e and S9. Compared to the data-free results (Figure 7d), the GPS data provide improved constraint on many parameters, so a priori bounds play a more limited role in influencing distributions. Distributions for chamber volume, initial pressure, centroid depth, aspect ratio, Υ, and compressibility are particularly improved relative to the "prior-only" case. The constraint on chamber volume comes in part from the time constant of the GPS data, and is in part an indirect result of the constraint on pressure at the top of the conduit, which places an upper bound on pressure change and therefore requires a large chamber (because of geodetic constraint on source strength (equation (17)). The large chamber volume in turn favors a small compressibility due to constraint by the time constant and extrusion data (equations (19) and (20)). Note also that conduit length and dissolved water have essentially the same distribution, scaled by pressure, because of pressure-solubility relationships.

[70] System compressibility again exhibits a strong peak associated with no exsolved water in the chamber, but the upper bound is much better constrained, in part due to GPS-constrained limits on L_{cc} in equation (22). Constraints on volatile content and Λ are from prior bounds, as before, and not the data.

[71] We can also compare results with those obtained using the same data but the analytical forward model (Figure 7b). The physics-based model provides improved constraint on chamber volume, pressure change, and conduit length, but other distributions are only modestly different. Since both inversions use the same data, improved constraints must come from additional prior bounds used in the more complex physics-based model. For example, large pressure changes are strongly limited by the prior constraint on pressure at the base of the plug (Figure S9, box 1), which in turn limits small magma chambers because of geodetic constraint on $V_0\Delta p_{ch}$. The weight of the lava dome also produces an increasing back pressure (a little over 4 MPa assuming a 220 m dome with density of 2000 kg/m^3) which requires a minimum initial excess chamber pressure [*Mastin et al.*, 2009].

5.3.3. Inversion of GPS and Extrusion Data

[72] Inverting using both GPS and extrusion data results in a near-perfect fit to extrusion data and does not significantly alter the already-reasonable fit to GPS data, although the best-fitting time constant is significantly lower (Figure 9). The forward model is therefore quite capable of explaining syn-eruptive observations at MSH, excluding unmodeled wander at GPS stations.

[73] As in the analytical model, the addition of extrusion data provides a better constraint on compressibility (equation (22)), with large values no longer permitted; however, results still favor the minimum possible value (for no exsolved volatiles), which is significantly lower than the preferred value in the analytical inversion for GPS and extrusion data (Figure 7c). The reduction in compressibility in turn improves constraint on centroid depth and volume and pressure change (Figure 7f). Distributions are also changed by the time constant of the extrusion data, which is smaller and better resolved than for the GPS data; this in turn limits the product of volume, compressibility, and conduit length, and/or increases frictional parameters (see equation (20)), which may explain the larger scaled reference velocity Υ in Figure 7f. Note that the upper bound on conduit pressure is no longer playing a role in limiting distributions (Figure S10, box 1).

[74] While chamber volume and pressure change remain correlated (Figure S10, box 2), both are well enough resolved that they can be separately estimated.

[75] Intuitively, observations of lava extrusion should help to better constrain influx into the magma chamber. Here only minor rates of chamber influx (at the end of the eruption) are predicted; the histogram in Figure 7f shows few values over 0.1 m^3/sec, with a peak only a little higher than 10^{-4} m^3/sec. This suggests that chamber influx may have been relatively minor and was not necessary to explain observed differences between extruded volume and inferred volume change at depth [e.g., *Lisowski et al*., 2008].

5.3.4. Inversion With Post-Eruptive Data

[76] Post-eruptive GPS time series at MSH exhibit evidence of reinflation of the deep magmatic system and offer valuable constraint on rates of influx into the chamber. We assume that the magma chamber geometry does not change during the syn- and post-eruptive periods and invert for a single set of model parameters for both time periods. We add stations P694 and P703 to the inversion to better constrain post-eruptive deformation.

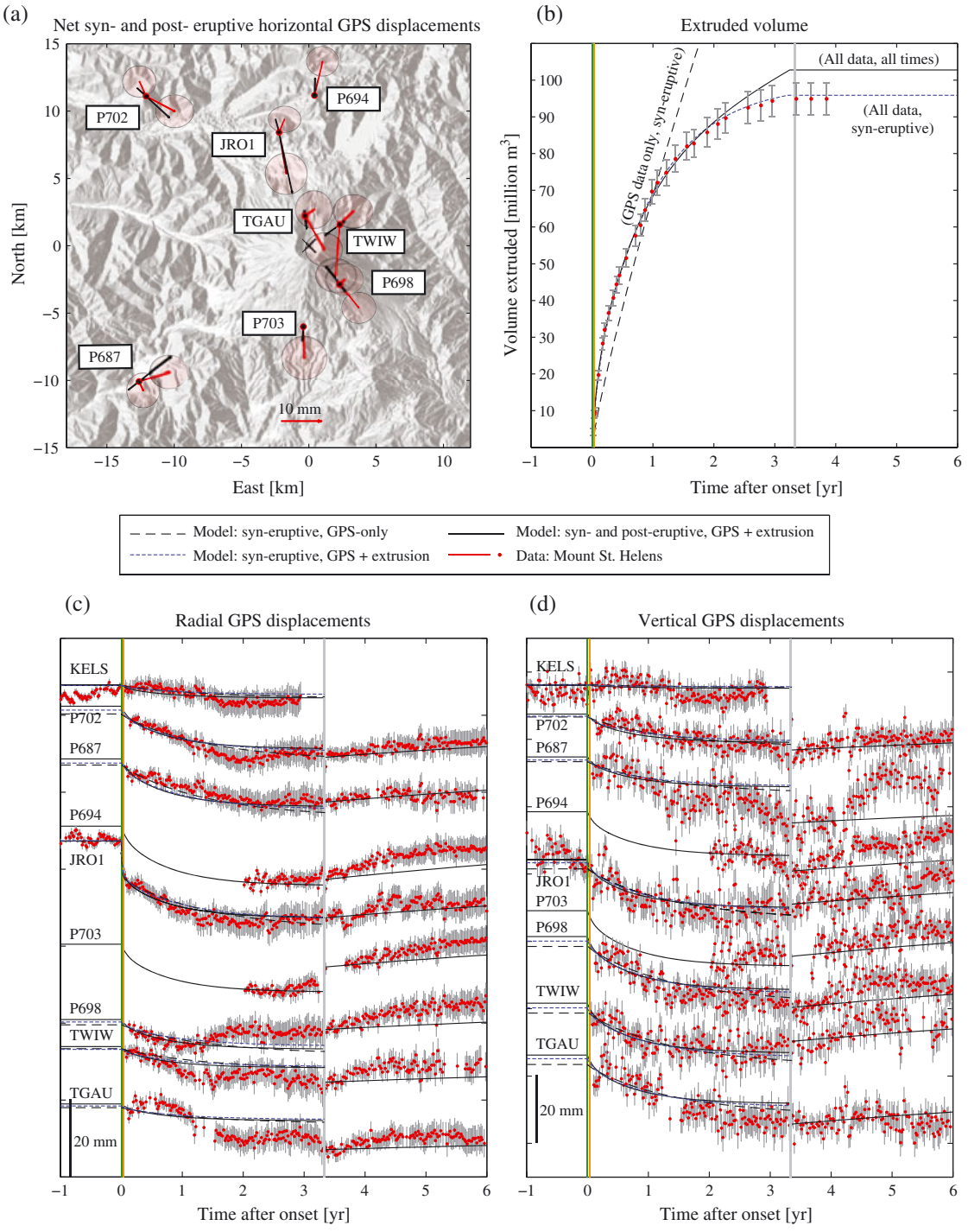

Figure 9. Fit-to-data for physics-based models. (a, b, c, and d) are as described in Figure 6. Shown are inversions for syn-eruptive GPS data, syn-eruptive GPS and extrusion data, and syn- and post-eruptive GPS and extrusion data (only the fit for syn and post-eruptive data is shown in Figure 9a). The fit to GPS data is similar for all results, although the GPS-only inversion favors a somewhat larger time constant. Post-eruptive displacements are mostly under-predicted, and including post-eruptive data results in a relatively poor fit to late-eruption extrusion data.

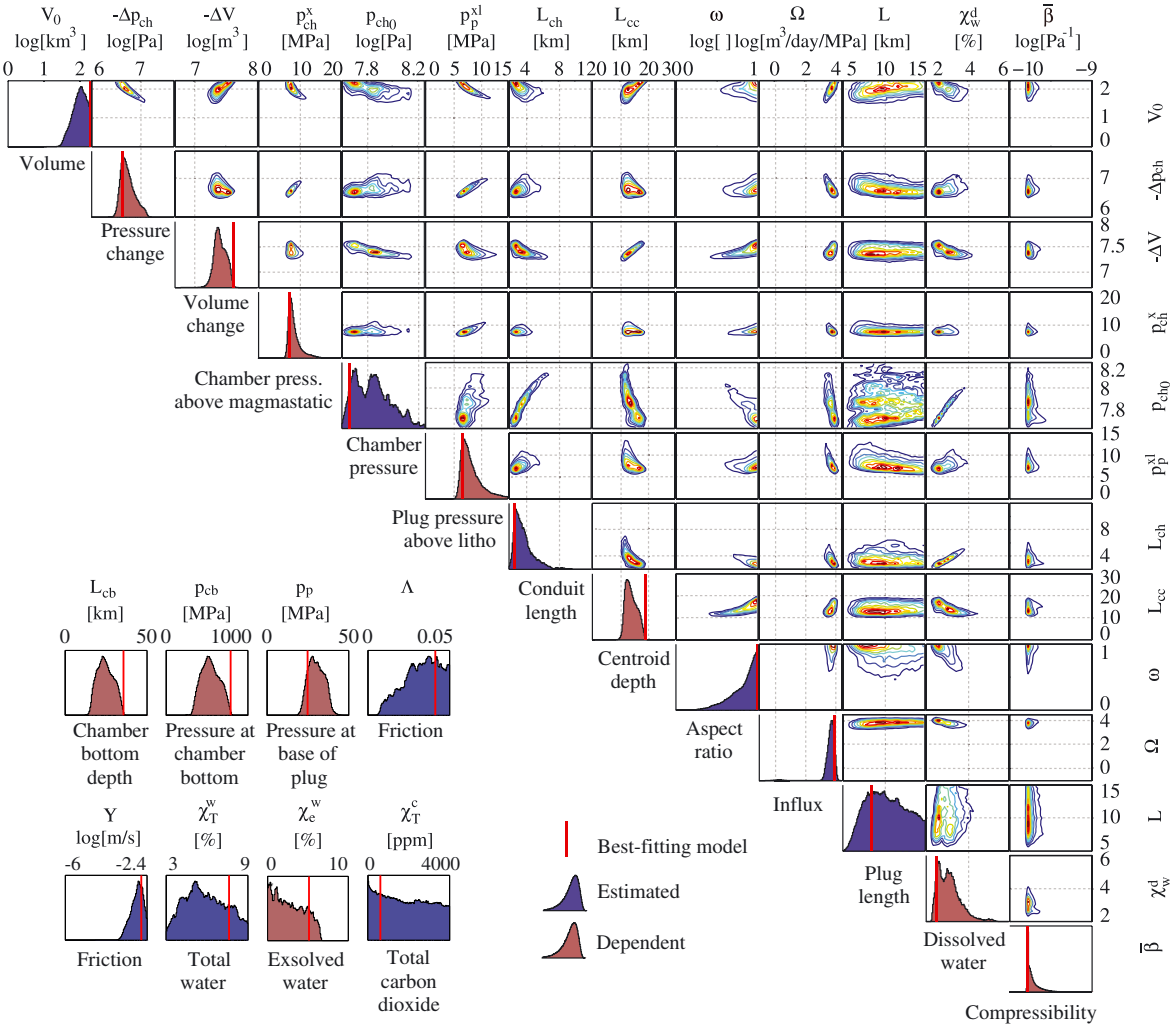

Figure 10. Posterior distributions derived from inversion of GPS and extrusion data using the physics-based model from Part 1, for both syn- and post-eruptive periods. Volume and pressure changes are shown for the syn-eruptive period only. See text for more information.

[77] Fits to data are shown in Figure 9. Syn-eruptive GPS time series are well-fit, but post-eruptive reinflation occurs more rapidly than predicted by the best-fitting model, and extrusion time series are not well-fit at the end of the eruption. This result suggests that the model of chamber influx is too simple and that a more complex process is at work. Note that higher rates of chamber influx cannot always be obtained by simply increasing the influx coefficient, because if the coefficient is too large then the pressure will not have dropped significantly over the eruption.

[78] Posterior distributions, which must be interpreted in light of the fact that the data are not well fit by the model, are shown in Figures 7g and 10. Post-eruptive data requires significant influx into the chamber, likely exceeding 0.2 m^3/sec at the end of the eruption (Figure 7g). The influx coefficient Ω is strongly correlated with pressure change (because more influx reduces pressure change) and by extension with initial pressure, so chamber pressure is somewhat smaller in this inversion. Low chamber pressures are in turn associated with short conduits, low dissolved water content, and a large aspect ratio (to yield the GPS-constrained centroid depth). As discussed in section 6.1, however, a 50 MPa chamber pressure with a top depth of 3 km is not consistent with independent observations, and distributions could be limited significantly by using less generous prior bounds.

6. Discussion

6.1. Results for Mount St. Helens

[79] We estimate the volume of the Mount St. Helens magma reservoir to be at least 40 km^3 with a poorly constrained upper bound (all discussion in this section is based on results from the physics-based syn-eruptive inversion of both GPS and extrusion data, and all bounds are at 95% unless otherwise noted). Independent estimates based on seismic, tomographic and other techniques vary widely from <1 to 20 km^3 or more [*Scandone and Malone*, 1985; *Barmin et al.*, 2002; *Pallister et al.*, 2008]. Using the expression $V_0 = V_f/\bar{\beta}p^x_{ch}$ (see equation (19)), constraining p^x_{ch} to be 10–20 MPa based on the height of the lava dome and rock strength around the chamber, and using a compressibility of $\bar{\beta} = 3.3 - 6.5 \times 10^{-10}$ Pa^{-1} inferred from differences between the extruded volume and source volume change,

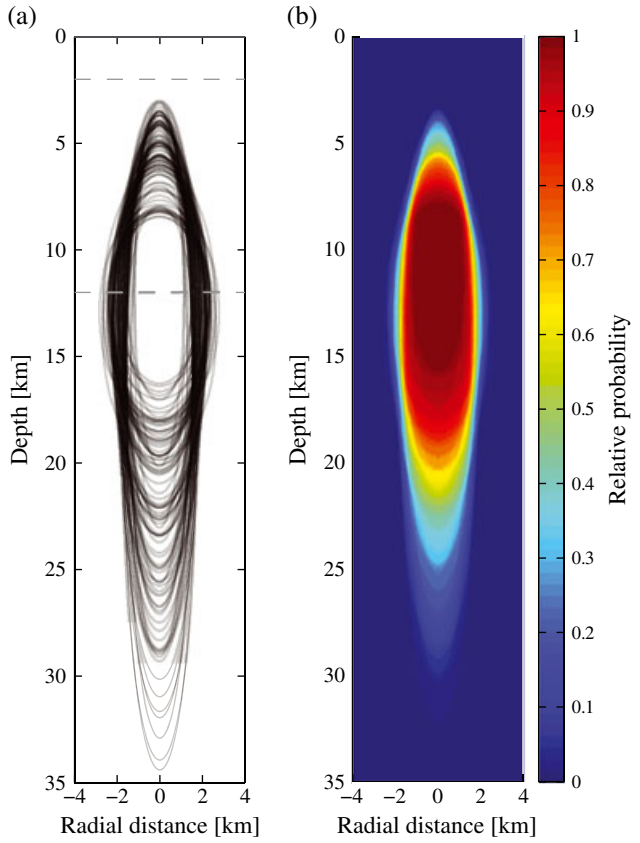

Figure 11. Probabilistic magma chamber geometry from syn-eruptive inversion using all data. Dashed horizontal lines indicate a priori bounds on chamber top depth. (a) Outline of 100 chambers selected randomly from MCMC results. (b) Relative probability of finding magma in a cross section through the crust beneath MSH, obtained by summing 2500 randomly selected magma chamber geometries from MCMC results. A roughly 2 km wide region between 8 and 16 km depth is included in almost every magma chamber accepted in the MCMC algorithm.

Mastin et al. [2009] estimated a volume of between 8 and 31 km^3. The compressibility estimated in this study ($1.6–4.0\times10^{-10}$ Pa^{-1} at $t = 0$) is smaller than in *Mastin et al.* [2009], which partly explains the larger chamber volume estimated here using similar data. Some other estimates may be biased towards volumes that are too small due to an inability to well-resolve the base of the chamber, and very small volumes may not be compatible with the largest eruptions at MSH over the last several thousand years of roughly 4 km^3 [*Carey et al.*, 1995], or with petrologic evidence of convection in the reservoir [*Rutherford and Devine*, 2008], and may also imply unrealistically large pressure changes in order to produce observed ground deformation. In general, however, this estimate is larger than most others, and while results need to be confirmed using a more sophisticated forward model and more restrictive prior bounds (see sections 6.2 and 6.3), has important implications if real (since, for instance, reservoir volume limits the maximum size of eruptions).

[80] We estimate that the centroid of the MSH magma reservoir lies at a depth of between 11–18 km beneath the crater floor, while independent estimates from inversion of geodetic data alone suggest a depth of about 8–9.5 km [*Lisowski et al.*, 2008; *Lisowski and Battaglia*, 2011; *Palano et al.*, 2012]. These differences are almost certainly due to the fewer number of stations used in our study, as well as some differences with GPS post-processing techniques; *Palano et al.* [2012] also uses only the first year of syn-eruptive data, exclusive of the vent-clearing phase.

[81] Our results suggest an elongate chamber with aspect ratio of at least 2 (the upper bound is not resolved within a priori bounds), in general agreement with geodetic estimates from *Lisowski and Battaglia* [2011] that the syn and post-eruptive sources had aspect ratios of 5.3 and 8.3, respectively. Inversions using geodetic data and simple kinematic models are unable to resolve the depth of the top of the magma reservoir, but we are able to estimate a depth of between 2.9 and 8.3 km below the crater floor. Seismic and other estimates suggest a depth of roughly 7–12 km [*Scandone and Malone*, 1985; *Moran*, 1994; *Pallister et al.*, 1992; *Musumeci et al.*, 2002; *Waite and Moran*, 2009], very similar to the centroid depths estimated from geodetic data and suggesting the degree of uncertainty in these estimates.

[82] A more intuitive way to visualize the estimated MSH chamber geometry and its uncertainty is shown in Figure11a. By randomly selecting sets of parameters from the MCMC results and plotting the corresponding reservoir shapes, it can be seen that most magma chambers consistent with the data and prior information are vertically elongate with a poorly constrained bottom depth but a well-defined width. By stacking a large number of chambers, it is possible to estimate the relative probability of finding magma at a given location in the crust. Figure 11b shows that there is a zone roughly 2 km wide between 8 and 16 km depth which includes magma in nearly all accepted models, and is very likely to lie within the MSH magma chamber.

[83] We estimate a pressure at the top of the magma chamber of between 50 and 170 MPa, while plagioclase equilibration data suggest pressures here of 120–140 MPa [*Rutherford and Devine*, 2008]. At the bottom of the chamber, we estimate a pressure of 340–740 MPa (assuming a constant magmastatic density in the chamber), while experimental work on amphiboles suggests that magma entered the storage chamber at ∼300 MPa [*Rutherford and Devine*, 2008]. The depth to the base of the chamber is not well resolved tomographically [*Waite and Moran*, 2009], but we are able to estimate a rough depth of 19–29 km.

[84] Results suggest a volume loss over the course of the eruption, exclusive of the vent-clearing phase, of 16–40 million m^3. These results agree with estimates by *Lisowski et al.* [2008] of 28 ± 5 million m^3.

[85] Results suggest a pressure at the base of the plug at the onset of the eruption of 21–39 MPa, while dacite samples from early in the eruption contained tridymite and exhibited a groundmass texture of holocrystalline quartz and feldspar intergrowth which suggest crystallization of the ascending magma at roughly 10–25 MPa over a period of weeks [*Cashman et al.*, 2008]. The length of the solid plug at MSH is not well constrained in this study, but results are generally consistent with drumbeat earthquake source depths of < 1km, assuming the drumbeats occurred along the margins of the slipping plug [e.g., *Iverson et al*. 2006].

[86] At the top of the chamber, at the conditions of last equilibration, we are able to estimate a dissolved water concentration of 2.6–4.9 wt%. Phase assemblages and compositions of rocks erupted from MSH over the last 4000 years indicate a wide range of water concentrations, from 3.7 to 6.5 wt% [*Rutherford and Devine*, 1988; *Gardner et al.*, 1995]. Few melt inclusions are available for the 2004–2008 eruption, but modeling by *Gerlach et al.* [2008] beginning with a total water concentration of 5 wt% at 220 MPa suggests a dissolved water concentration at the top of the chamber of around 4.4 wt% (along with a total CO_2 concentration of approximately 2000 ppm). Total water and CO_2 concentrations are poorly constrained in this study. Although CO_2 can play an important role in eruptive activity it is not well resolved because of correlation with total water content, and because we do not here use observations of gas emissions.

6.2. Further Restricting Posterior Distributions

[87] Using the Bayesian approach outlined in this study, independent estimates of model parameters and properties can be used not only to compare to inversion results as in the previous section but also as a priori constraints to directly inform final posterior distributions. For example, the aspect ratio of the chamber could be constrained using earthquake hypocenters and tomography, and the volatile content constrained using petrologic estimates.

[88] As a simple test of this approach, we apply an a priori constraint on dissolved water of $\chi_d^w > 3.5$ wt%. Rather than rerunning the inversion, as a quick test, we simply use existing results and set $P = 0$ for $\chi_d^w < 3.5$ wt%. This constraint results in distributions for chamber top pressure and depth that are higher and deeper, respectively (shallow, low-pressure chambers are not compatible with high volatile content), and a distribution for aspect ratio that favors less elongate chambers (because of geometrical relationships between depth and aspect ratio). Applying more restrictive prior bounds may thus significantly improve estimates of other parameters.

6.3. Assumptions and Influence on Results

[89] Assumptions made in the formulation of the forward model (detailed more fully in Part 1) must influence posterior distributions and may explain some of the differences between our estimates and independent estimates.

[90] The assumption of a spheroidal magma chamber embedded in a purely elastic medium and connected to the surface with a cylindrical vertical conduit is certainly too simplistic, although as discussed in section 4.2, may be correct to at least first order. We do clearly oversimplify in extrapolating density and pressure from the top of the chamber to its centroid depth, not accounting for changes in density, phenocryst content, and other properties of the melt. Also, if the magma chamber contains independent (or partially independent) pressure compartments [e.g., *Gudmundsson*, 2012] then inversion results might be insensitive to some parts of the chamber.

[91] The conduit is modeled as a cylinder of constant radius, crystallization depth does not respond to changes in conduit pressure, and gas loss is not modeled. Conduits of a more irregular shape would presumably provide more resistance to flow, and if the modeled crystallization depth changed over the course of an eruption, it would probably reduce estimates of extruded volume and geodetic displacements and also influence the predicted time constant. The assumption of no gas loss is probably reasonable for most of the fluid conduit, but is less so at shallower depths where increased wall rock permeability and gas volume fractions favor degassing (gas loss must occur, because observed dome rock porosities are significantly lower than porosities modeled in the upper conduit); as a result, modeled conduit densities are probably too low and vertical velocities too high. Inversions suggest average fluid conduit densities of well under 2000 kg/m^3, resulting in a magmastatic gradient much lower than lithostatic. Because we limit pressure at the base of the plug to roughly lithostatic, pressures at the top of the chamber can be below lithostatic, in turn biasing chamber pressure to be too low and compressibility to be too high. Observations from a number of eruptions suggest that upper conduit or internal dome pressures for explosive eruptions of lava domes are often in the range of 1–20 MPa, while excess magma chamber pressures are often 5–20 MPa (roughly the strength of the host rock) [*Sparks*, 1997]. These numbers can only be reconciled with one another with a more nonlinear pressure gradient and/or a higher density of magma in the conduit than calculated in our forward model, and suggest that neglecting gas loss must bias some of the parameters estimated in this study.

[92] The term that accounts for rapid early displacement at JRO1 associated with vent clearing processes (section 4.2) means that part of the total pressure change in the chamber is not accounted for in posterior distributions. Furthermore, because we add the vent-clearing term to displacements but not extruded volumes, compressibility estimates may be biased, although the magnitude of the bias depends on the nature of the vent-clearing processes and is unknown.

[93] The model imperfectly predicts both syn- and post-eruptive data with a single set of model parameters. Our model of chamber influx linearly proportional to pressure difference is likely too simple.

[94] Enforcing the end of the eruption at a fixed time is usually reasonable because the data constrain extrusion rate is to be very low near the end of the eruption anyway. However, models which poorly fit the extrusion data may be forced to end even if they predict large extrusion rates at the observed end of the eruption. This problem might be resolved by including a yield strength in the conduit, such that the eruption would stop before the pressure drops to magmastatic; however, such work is saved for future consideration.

6.4. Comments on Uncertainty

[95] In this work we have attempted to carefully estimate the uncertainties associated with model parameters. However, the resulting posterior PDFs almost certainly underestimate uncertainty because of the following: (1) they do not account for the forward model being an imperfect representation of the volcanic system ("model uncertainty"), (2) they do not account for variations in results due to the choice of data or post-processing techniques (see section S1), (3) estimates of noise in data are imperfect, and (4) by fixing model parameters such as shear modulus and conduit radius in the inversions, we fail to account for uncertainty in these parameters.

[96] Many of these uncertainties are very difficult to quantify. Inversions including more parameters could reduce the impact of (4), although at the cost of additional computation time. This effect could be significant. For instance, shear modulus is inversely proportional to ground displacements (equation (12)), so if we fix shear modulus at a value half of that which is appropriate, ground displacements will be overpredicted by a factor of two, with a resulting bias in estimates of compressibility and other parameters. Results are even more sensitive to conduit radius R, to which conduit conductivity (in the simple analytical model) is sensitive to the fourth power: $c = \pi R^4/8\bar{\eta}L_{\mathrm{ch}}$. When possible, it is therefore warranted to estimate additional parameters even if they are not of direct interest.

[97] In general, it should be remembered that posterior PDFs represent uncertainty only for the combination of prior constraints, data, and forward model chosen, and they are almost certainly minima.

7. Conclusions

[98] A physics-based model of a volcanic eruption can be used to relate observations from many different disciplines in a common framework, and in a Bayesian inverse procedure, can be combined with independent information to obtain probabilistic estimates of key properties of the volcanic system. This approach carries a number of significant advantages over the more traditional approach of inverting deformation data using kinematic forward models. With the technique outlined in this study, diverse observations can be used to constrain otherwise difficult to estimate properties of a volcanic system, such as the absolute volume of the magma chamber and properties of the melt (which carry obvious implications for hazard assessment).

[99] In this study we use a physics-based model of the effusive 2004–2008 eruption of Mount St. Helens which is able to predict observed lava dome extrusion and ground deformation time series. We compare inversions using the physics-based forward model with an inversion using a model of a kinematic magma chamber, and with inversions using a model of a deflating elastic reservoir. We find that many important properties of the volcanic system cannot be independently obtained with the simpler models, but with physics-based models and both the extrusion and deformation time series, it is possible to place constraint on the absolute volume of the magma chamber, its pressure and volume change, its centroid depth, and the water content of melt in the chamber. Other parameters such as chamber pressure and conduit length are less well resolved because they are strongly correlated with one another, but given some constraint on one, the other could be independently resolved. Post-eruptive data provides valuable additional constraint on chamber influx and many other related parameters, although an imperfect fit to data when including the post-eruptive time period indicates that the model of chamber influx used in this study is too simple.

[100] Results for Mount St. Helens must be evaluated with consideration of assumptions implicit in the forward model, such as no gas loss from the fluid conduit and the use of only weakly informative prior information. Many parameters, however, such as chamber aspect ratio and dissolved water content at the top of the chamber (2.6–4.9 wt%) are generally consistent with independent estimates. Our results do suggest a larger magma chamber than commonly believed to exist beneath MSH (>40 km^3) with a correspondingly shallower top depth (∼3–8 km), and a deeper centroid depth (11–18 km). The length and frictional behavior of the solid plug is poorly constrained, as is magma carbon dioxide content. We calculate a very high probability of magma residing between 8 and 16 km below the crater floor with a width of roughly 2 km. Future work involving a more sophisticated forward model (including gas loss and crystallization processes), incorporating additional prior information or tighter prior bounds into the inverse procedure, and constrained by additional data sets such as gas emissions and gravity changes, should allow us to significantly improve on these estimates.

[101] Although computationally and conceptually more demanding than optimizations using simple kinematic forward models, the inverse approach outlined in this study offers significant advantages over more common techniques. With continued improvements in the quantity and quality of data recorded at erupting volcanoes, along with increases in computational power, we believe that probabilistic inversions using physics-based models will become an increasingly important tool for interpreting observations and understanding volcanic systems.

Appendix A: Friction

[102] The value of frictional parameter a is thought to be strongly temperature-dependent [*Blanpied et al.*, 1995]. Thermal imaging of the extruded spines at MSH recorded surface temperatures of about 200°C where they emerged from the vent and temperatures of over 700°C in fractured regions [*Schneider et al.*, 2008]. However, *Moore et al.* [2008] noted that gouge samples from early 2005 were cool and noncohesive, and argued that the frictional behavior of the gouge was probably similar to low-temperature gouge in shallow crustal faults. Over temperatures of 100°C–800°C, data in *Blanpied et al.* [1995] for wet and dry granite gouge suggest $a - b$ could vary from < 0 to >0.04 (b governs the evolution effect: see the discussion in Part 1, Appendix A4). We use $0 \leq a \leq 0.06$ ($b = 0$ in our steady-state friction model).

[103] The nominal coefficient of friction f_0 for MSH fault gouge was estimated in steady-state experiments to be approximately 0.42 to 0.47 at room temperature and low normal stress (< 1 MPa) [*Iverson et al.*, 2006; *Moore et al.*, 2008]. At higher pressures, experiments on granite suggest $f_0 \approx 0.6$ to 0.8 at >300 MPa [*Blanpied et al.*, 1998] (MSH laboratory values may be lower partly due to the presence of fault gouge, which may significantly reduce the coefficient of friction [*Byerlee*, 1978]). We constrain $0.1 \leq f_0 \leq 0.8$.

[104] Finally, we use a normal stress coefficient of $0.3 \leq \sigma_c \leq 1$ modified from *Mastin et al.* [2008] and a pore pressure coefficient of $0.25 \leq \zeta \leq 1$.

[105] With these uniform prior constraints and a reference velocity v_r set to roughly the initial extrusion rate of 0.001 m/s, $0 < \Lambda < 0.05$ and $0 < \Upsilon < 2\times10^{-4}$ m/s. However, inversions indicate that a larger Υ is needed to adequately fit the data, so we use an upper bound of 0.004 m/s.

[106] **Acknowledgments.** Mike Lisowski and Noel Bartlow provided valuable assistance with GPS data post-processing. We appreciate valuable reviews from Larry Mastin and two anonymous reviewers, as well as comments from the Associate Editor. This work was supported by NSF grant EAR-0910708.

References

Anderson, K., and P. Segall (2011), Physics-based models of ground deformation and extrusion rate at effusively erupting volcanoes, *J. Geophys. Res.*, *116*, B07,204–, doi:10.1029/2010JB007939.

Anderson, K., M. Lisowski, and P. Segall (2010), Cyclic ground tilt associated with the 2004–2008 eruption of Mount St. Helens, *J. Geophys. Res.*, *115*, B11,201–, doi:10.1029/2009JB007102.

Barmin, A., O. Melnik, and R. S. J. Sparks (2002), Periodic behavior in lava dome eruptions, *Earth Planet. Sci. Lett.*, *199*, 173–184, doi:10.1016/S0012-821X(02)00557-5.

Blanpied, M. L., D. A. Lockner, and J. D. Byerlee (1995), Frictional slip of granite at hydrothermal conditions, *J. Geophys. Res.*, *100*, 13, doi:10.1029/95JB00862.

Blanpied, M. L., C. J. Marone, D. A. Lockner, J. D. Byerlee, and D. P. King (1998), Quantitative measure of the variation in fault rheology due to fluid-rock interactions, *J. Geophys. Res.*, *103*(B5), 9691–9712, doi:10.1029/98JB00162.

Byerlee, J. (1978), Friction of rocks, *Pure Appl. Geophys.*, *116*, 615–626, doi:10.1007/BF00876528, 10.1007/BF00876528.

Carey, S., and H. Sigurdsson (1985), The May 18 eruption of Mount St. Helens. 2. Modeling of dynamics of the Plinian phase, *J. Geophys. Res.*, *90*, 2948–2958, doi:10.1029/JB090iB04p02948.

Carey, S., J. Gardner, and H. Sigurdsson (1995), The intensity and magnitude of Holocene plinian eruptions from Mount St. Helens volcano, *J. Volcanol. Geotherm. Res.*, *66* (1-4), 185–202, doi:10.1016/0377-0273(94)00059-P.

Cashman, K. V., C. R. Thornber, and J. S. Pallister (2008), From dome to dust: shallow crystallization and fragmentation of conduit magma during the 2004–2006 dome extrusion of Mount St. Helens, Washington, A volcano rekindled: The renewed eruption of Mount St. Helens, 2004–2006, U.S. Geological Survey Professional Paper 1750.

Costa, A. (2005), Viscosity of high crystal content melts: Dependence on solid fraction, *Geophys. Res. Lett.*, *32*, L22308, doi:10.1029/2005GL024303.

Costa, A., O. Melnik, R. Sparks, and B. Voight (2007), Control of magma flow in dykes on cyclic lava dome extrusion, *Geophys. Res. Lett.*, *34*, L02303, doi:10.1029/2006GL027466.

Dzurisin, D., M. Lisowski, M. Poland, D. R. Sherrod, and R. G. LaHusen (2008), Constraints and conundrums posed by Ground Deformation Measurements during the 2004–2005 dome-building eruption of Mount St. Helens, Washington, A volcano rekindled: The renewed eruption of Mount St. Helens, 2004–2006, U.S. Geological Survey Professional Paper 1750.

Fukuda, J., and K. Johnson (2008), A fully Bayesian inversion for spatial distribution of fault slip with objective smoothing, *Bull. Seismol. Soc. Am.*, *98*, 1128–1146, doi:10.1785/0120070194.

Gamerman, D., and H. Lopes (2006), *Markov Chain Monte Carlo: Stochastic Simulation for Bayesian Inference*, 323 pp., Chapman and Hall/CRC, Boca Raton, Fla.

Gardner, J. E., M. Rutherford, S. Carey, and H. Sigurdsson (1995), Experimental constraints on pre-eruptive water contents and changing magma storage prior to explosive eruptions of Mount St Helens volcano, *Bull. Volcanol.*, *57*, 1–17, doi:10.1007/BF00298703.

Gerlach, T. M., K. A. McGee, and M. P. Doukas (2008), Emission Rates of CO_2, SO_2, and H_2S, scrubbing, and preeruption excess volatiles at Mount St. Helens, 2004–2005, A volcano rekindled: The renewed eruption of Mount St. Helens, 2004–2006, U.S. Geological Survey Professional Paper 1750.

Green, D. N., J. Neuberg, and V. Cayol (2006), Shear stress along the conduit wall as a plausible source of tilt at Soufriere Hills Volcano, Montserrat, *Geophys. Res. Lett.*, *33*, L10306, doi:10.1029/2006GL025890.

Gudmundsson, A. (2012), Magma chambers: Formation, local stresses, excess pressures, and compartments, *J. Volcanol. Geotherm. Res.*, *237-238*, 19–41, doi:10.1016/j.jvolgeores.2012.05.015.

Hastings, W. K. (1970), Monte Carlo sampling methods using Markov chains and their applications, *Biometrika*, *57*(1), 97–109.

Hess, K. U., and D. B. Dingwell (1996), Viscosities of hydrous leucogranitic melts: A non-Arrhenian model, *Am. Mineral.*, *81*(9-10), 1297–1300.

Huppert, H., and A. Woods (2002), The role of volatiles in magma chamber dynamics, *Nature*, *420*, pp. 493–495, doi:10.1038/nature01211.

Iverson, R. M., et al. (2006), Dynamics of seismogenic volcanic extrusion at Mount St. Helens in 2004–05, *Nature*, *444*, 439–443, doi:10.1038/nature05322.

Jaupart, C. (1996), Physical models of volcanic eruptions, *Chem. Geol.*, *128*(1-4), 217–227, doi:10.1016/0009-2541(95)00175-1.

Lisowski, M., and M. Battaglia (2011), Modeling deformation associated with the 2004–2008 dome-building eruption of Mount St. Helens, Abstract V33C-2650, American Geophysical Union Fall Meeting 2011.

Lisowski, M., D. Dzurisin, R. P. Denlinger, and E. Y. Iwatsubo (2008), Analysis of GPS-measured deformation associated with the 2004–2006 dome-building eruption of Mount St. Helens, Washington, A volcano rekindled: The renewed eruption of Mount St. Helens, 2004–2006, U.S. Geological Survey Professional Paper 1750.

Liu, Y., Y. Zhang, and H. Behrens (2005), Solubility of H_2O in rhyolitic melts at low pressures and a new empirical model for mixed H_2O-CO_2 solubility in rhyolitic melts, *J. Volcanol. Geotherm. Res.*, *143*, 219–235, doi:10.1016/j.jvolgeores.2004.09.019, Volcanic Eruption Mechanisms - Insights from intercomparison of models of conduit processes.

Massol, H., C. Jaupart, and D. W. Pepper (2001), Ascent and decompression of viscous vesicular magma in a volcanic conduit, *J. Geophys. Res.*, *106*(B8), 16,223–16,240, doi:10.1029/2001JB000385.

Mastin, L., M. Lisowski, E. Roeloffs, and N. Beeler (2009), Improved constraints on the estimated size and volatile content of the Mount St. Helens magma system from the 2004–2008 history of dome growth and deformation, *Geophys. Res. Lett.*, *36*, L20,304, doi:10.1029/2009GL039863.

Mastin, L. G., and M. S. Ghiorso (2000), A numerical program for steady-state flow of magma-gas mixtures through vertical eruptive conduits, 56 pp., U.S. Geological Survey Open-File Report 00-209.

Mastin, L. G., E. Roeloffs, N. M. Beeler, and J. E. Quick (2008), Constraints on the size, overpressure, and volatile content of the Mount St. Helens magma system from geodetic and dome-growth measurements during the 2004–2006+ eruption, A volcano rekindled: The renewed eruption of Mount St. Helens, 2004–2006, U.S. Geological Survey Professional Paper 1750.

McTigue, D. F. (1987), Elastic stress and deformation near a finite spherical magma body: Resolution of the point source paradox, *J. Geophys. Res.*, *92*, 12,931–12,940, doi:10.1029/JB092iB12p12931.

Melnik, O., and R. S. J. Sparks (1999), Nonlinear dynamics of lava dome extrusion, *Nature*, *402*, 37–41, doi:10.1038/46950.

Melnik, O., and R. S. J. Sparks (2005), Controls on conduit magma flow dynamics during lava dome building eruptions, *J. Geophys. Res.*, *110*, B02209, doi:10.1029/2004JB003183.

Metropolis, N., A. W. Rosenbluth, M. N. Rosenbluth, A. H. Teller, and E. Teller (1953), Equation of state calculations by fast computing machines, *J. Chem. Phys.*, *21*(6), 1087–1092, doi:10.1063/1.1699114.

Moore, P. L., N. R. Iverson, and R. M. Iverson (2008), Frictional properties of the Mount St. Helens gouge, A volcano rekindled: The renewed eruption of Mount St. Helens, 2004–2006, U.S. Geological Survey Professional Paper 1750.

Moran, S. C. (1994), Seismicity at Mount St. Helens, 1987–1992: Evidence for repressurization of an active magmatic system, *J. Geophys. Res. Solid Earth*, *99*(B3), 4341–4354, doi:10.1029/93JB02993.

Moran, S. C., S. D. Malone, A. I. Qamar, W. A. Thelen, A. K. Wright, and J. Caplan-Auerbach (2008), Seismicity associated with renewed dome building at Mount St. Helens, 2004–2005, avolcano rekindled: The renewed eruption of Mount St. Helens, 2004–2006, U.S. Geological Survey Professional Paper 1750.

Mosegaard, K., and A. Tarantola (1995), Monte Carlo sampling of solutions to inverse problems, *J. Geophys. Res.*, *100*, 12,431–12,447.

Mosegaard, K., and A. Tarantola (2002), Probabilistic approach to inverse problems, in *International Handbook of Earthquake and Engineering Seismology,* vol. 81A, edited by P. C. J. William, H. K. Lee, H. Kanamori, and C. Kisslinger, pp. 237–265, Academic Press, Amsterdam, doi:10.1016/S0074-6142(02)80219-4.

Musumeci, C., S. Gresta, and S. D. Malone (2002), Magma system recharge of Mount St. Helens from precise relative hypocenter location of microearthquakes, *J. Geophys. Res. Solid Earth*, *107*(B10), 2264–2272, doi:10.1029/2001JB000629.

Palano, M., E. Guarrera, and M. Mattia (2012), GPS ground deformation patterns at Mount St. Helens (Washington, USA) from 2004 to 2010, *Terra Nova*, *24*, 148–155, doi:10.1111/j.1365-3121.2011.01049.X.

Pallister, J. S., R. P. Hoblitt, D. R. Crandell, and D. R. Mullineaux (1992), Mount St. Helens a decade after the 1980 eruptions: Magmatic models, chemical cycles, and a revised hazards assessment, *Bull. Volcanol.*, *54*, 126–146, doi:10.1007/BF00278003.

Pallister, J. S., C. R. Thornber, K. V. Cashman, M. A. Clynne, H. A. Lowers, C. W. Mandeville, I. K. Brownfield, and G. P. Meeker (2008), Petrology of the 2004–2006 Mount St. Helens lava dome—implications for magmatic plumbing and eruption triggering, A volcano rekindled:

The renewed eruption of Mount St. Helens, 2004–2006, U.S. Geological Survey Professional Paper 1750.

Poland, M. P., and Z. Lu (2008), Radar interferometry observations of surface displacements during pre- and co-eruptive periods at Mount St. Helens, Washington, 1992–2005, A volcano rekindled: The renewed eruption of Mount St. Helens, 2004–2006, U.S. Geological Survey Professional Paper 1750.

Rutherford, M. J., and J. D. Devine (1988), The May 18, 1980, eruption of Mount St. Helens 3. Stability and chemistry of amphibole in the magma chamber, *J. Geophys. Res.*, *93* (B10), 11,949–11,959, doi:10.1029/JB093iB10p11949.

Rutherford, M. J., and J. D. Devine (2008), Magmatic conditions and processes in the storage zone of the 2004–2006 Mount St. Helens dacite, A volcano rekindled: The renewed eruption of Mount St. Helens, 2004–2006, U.S. Geological Survey Professional Paper 1750.

Sambridge, M., and K. Mosegaard (2002), Monte Carlo methods in geophysical inverse problems, *Rev. Geophys.*, *40*(3), 1009–, doi:10.1029/2000RG000089.

Scandone, R., and S. D. Malone (1985), Magma supply, magma discharge and readjustment of the feeding system of Mount St. Helens during 1980, *J. Volcanol. Geotherm. Res.*, *23*(3-4), 239–262, doi:10.1016/0377-0273(85)90036-8.

Schilling, S. P., R. A. Thompson, J. A. Messerich, and E. Y. Iwatsubo (2008), Use of digital aerophotogrammetry to determine rates of lava dome growth, Mount St. Helens, 2004–2005, A volcano rekindled: The renewed eruption of Mount St. Helens, 2004–2006, U.S. Geological Survey Professional Paper 1750.

Schneider, D. J., J. W. Vallance, R. L. Wessels, M. Logan, and M. S. Ramsey (2008), Use of thermal infrared imaging for monitoring renewed dome growth at Mount St. Helens, 2004, A volcano rekindled: The renewed eruption of Mount St. Helens, 2004–2006, U.S. Geological Survey Professional Paper 1750.

Scholz, C. (1998), Earthquakes and friction laws, *Nature*, *39*, 37–42, doi:10.1038/34097.

Scott, W. E., D. R. Sherrod, and C. A. Gardner (2008), Overview of the 2004 to 2006, and continuing, eruption of Mount St. Helens, Washington, A volcano rekindled: The renewed eruption of Mount St. Helens, 2004–2006, U.S. Geological Survey Professional Paper 1750.

Segall, P. (2010), *Earthquake and Volcano Deformation*, 432 pp., Princeton University Press, Princeton, NJ.

Segall, P. (2013), Volcano deformation and eruption forecasting, Geological Society, London, Special Publications, doi:10.1144/SP380.4, in press.

Segall, P., P. Cervelli, S. Owen, M. Lisowski, and A. Miklius (2001), Constraints on dike propagation from continuous GPS measurements, *J. Geophys. Res.*, *106*(B9), 19,301–19,317, doi:10.1029/2001JB000229.

Sparks, R. S. J. (1997), Causes and consequences of pressurisation in lava dome eruptions, *Earth Planet. Sci. Lett.*, *150* (3-4), 177–189, doi:10.1016/S0012-821X(97)00109-X.

Stasiuk, M. V., C. Jaupart, and R. S. J. Sparks (1993), On the variations of flow-rate in nonexplosive lava eruptions, *Earth Planet. Sci. Lett.*, *114*(4), 505–516, doi:10.1016/0012-821X(93)90079-O.

Thelen, W. A., R. S. Crosson, and K. C. Creager (2008), Absolute and relative locations for earthquakes at Mount St. Helens, Washington using continuous data: Implications for magmatic processes, A volcano rekindled: The renewed eruption of Mount St. Helens, 2004–2006, U.S. Geological Survey Professional Paper 1750.

Timoshenko, S., and J. Goodier (1970), *Theory of Elasticity*, McGraw-Hill, New York.

Vallance, J. W., D. J. Schneider, and S. P. Schilling (2008), Growth of the 2004–2006 lava-dome complex at Mount St. Helens, Washington, A volcano rekindled: The renewed eruption of Mount St. Helens, 2004–2006, U.S. Geological Survey Professional Paper 1750.

Wadge, G. (1981), The variations of magma discharge during basaltic eruptions, *J. Volcanol. Geotherm. Res.*, *11*(2-4), 139–168, doi:10.1016/0377-0273(81)90020-2.

Waite, G. P., and S. C. Moran (2009), Vp structure of Mount St. Helens, Washington, USA, imaged with local earthquake tomography, *J. Volcanol. Geotherm. Res.*, *182*, 113–122, doi:10.1016/j.jvolgeores.2009.02.009.

Waite, G. P., B. A. Chouet, and P. B. Dawson (2008), Eruption dynamics at Mount St. Helens imaged from broadband seismic waveforms: Interaction of the shallow magmatic and hydrothermal systems, *J. Geophys. Res. Solid Earth*, *113*, B02305, doi:10.1029/2007JB005259.

Williams, D. L., G. Abrams, C. Finn, D. Dzurisin, D. J. Johnson, and R. Denlinger (1987), Evidence from gravity data for an intrusive complex beneath Mount St. Helens, *J. Geophys. Res.*, *92*(B10), 10,207–10,222, doi:10.1029/JB092iB10p10207.

Woods, A., and H. Huppert (2003), On magma chamber evolution during slow effusive eruptions, *J. Geophys. Res.*, *108*(B8), 2403, doi:10.1029/2002JB002019.

Yang, X. M., P. M. Davis, and J. H. Dieterich (1988), Deformation from inflation of a dipping finite prolate spheroid in an elastic half-space as a model for volcanic stressing, *J. Geophys. Res. Solid Earth Planets*, *93*(B5), 4249–4257, doi:10.1029/JB093iB05p04249.